Direct ink writing of sustainable multifunctional biodegradable porous Fe-eggshell scaffolds

Putra, Niko E.; Youf, Raphaëlle; Moosabeiki, Vahid; Leeflang, Marius A.; Klimopoulou, Maria; Mirzaali, Mohammad J.; Mol, Arjan; Riool, Martijn; Fratila-Apachitei, Lidy E.; Zhou, Jie

DOI
10.1016/j.actbio.2025.06.051

Publication date
2025

Document Version
Final published version

Published in
Acta Biomaterialia

Citation (APA)
Putra, N. E., Youf, R., Moosabeiki, V., Leeflang, M. A., Klimopoulou, M., Mirzaali, M. J., Mol, A., Riool, M., Fratila-Apachitei, L. E., Zhou, J., Apachitei, I., & Zadpoor, A. A. (2025). Direct ink writing of sustainable multifunctional biodegradable porous Fe-eggshell scaffolds. *Acta Biomaterialia*, *202*, 622-640. https://doi.org/10.1016/j.actbio.2025.06.051

Acta Biomaterialia 202 (2025) 622–640

Contents lists available at ScienceDirect

Acta Biomaterialia

journal homepage: www.elsevier.com/locate/actbio

Full length article

Direct ink writing of sustainable multifunctional biodegradable porous Fe-eggshell scaffolds

Niko E. Putra [a,*], Raphaëlle Youf [b], Vahid Moosabeiki [a], Marius A. Leeflang [a], Maria Klimopoulou [a], Mohammad J. Mirzaali [a], Arjan Mol [c], Martijn Riool [b], Lidy E. Fratila-Apachitei [a], Jie Zhou [a], Iulian Apachitei [a], Amir A. Zadpoor [a]

[a] Department of Biomechanical Engineering, Faculty of Mechanical Engineering, Delft University of Technology, Mekelweg 2, 2628 CD Delft, the Netherlands
[b] Department of Trauma Surgery, University Medical Center Regensburg, Franz-Josef- Strauß-Allee 11, 93053 Regensburg, Germany
[c] Department of Materials Science and Engineering, Faculty of Mechanical Engineering, Delft University of Technology, Mekelweg 2, 2628 CD Delft, the Netherlands

ARTICLE INFO

Keywords:
Additive manufacturing
Direct ink writing
Sustainable biomaterials
Iron-eggshell composite
Biodegradable implant
Bone substitution

ABSTRACT

Medical devices contribute to the carbon footprint generated by the healthcare sector. The development of implants and biomaterials using recycled waste materials promotes sustainable advances in tissue engineering. Additively manufactured (AM) bone-substituting biomaterials with multifunctional properties, *e.g.*, biodegradability, antibacterial and osteogenic potential, can contribute to sustainable healthcare. Biodegradable biomaterials eliminate secondary surgeries to remove implants, reduce post-surgical complications, and enhance patient recovery, thus decreasing the energy usage and waste associated with medical treatments. Herein, we present porous iron (Fe) scaffolds incorporating 20 vol% waste-derived eggshell particles for bone substitution. The Fe-eggshell scaffolds were fabricated using direct ink writing (DIW) technique and underwent post-AM heat treatment. During sintering, the eggshell's main component – $CaCO_3$, transformed into CaO. Atomic diffusion between α-Fe and CaO phases resulted in the formation of $Ca_2Fe_2O_5$ phase at the interface. The scaffolds were 70 % porous and displayed a biodegradation rate of 0.11 mm/year. The mechanical properties were comparable to trabecular bone and the scaffolds endured 3 million loading cycles at $0.7\sigma_y$ in r-SBF. The scaffolds showed apatite-forming ability, evidenced by the formation of (carbonaceous) hydroxyapatite, which are conducive to preosteoblast adhesion, proliferation, and differentiation. RT-qPCR analysis confirmed the osteogenic potential of the specimens as evidenced by the upregulated expression of osteopontin and osteocalcin as compared to Ti6Al4V controls. Furthermore, the scaffolds exhibited bactericidal activity (>3.9-log CFU reduction) against methicillin-sensitive and multidrug-resistant strains of *Staphylococcus aureus* and delayed their biofilm formation. Our research showcases the exceptional multifunctionality of DIW Fe-eggshell composite scaffolds for the sustainable development of orthopedic biomaterials.

Statement of significance: We aim to improve the biofunctionalities and sustainability of biodegradable bone substitutes, by developing the extrusion-based 3D printed porous Fe composite scaffolds containing eggshell-derived CaO bioceramics. Our results demonstrated that Fe-eggshell scaffolds exhibited hydroxyapatite-forming ability in simulated body fluid, having mechanical properties in the range of trabecular bone even after 4 weeks biodegradation, supported the proliferation of preosteoblasts and upregulated the expression of osteogenic genes. Moreover, the scaffolds were bactericidal against methicillin-sensitive and multi-drug resistant strains *Staphylococcus aureus* and delayed their biofilm formation.

1. Introduction

The development of sustainable biomaterials for medical devices and tissue engineering contributes to the reduction of the carbon footprint of the healthcare sector. The design of sustainable biomaterials can be realized by taking environmental factors into account all the way from the selection of raw materials to the selection of manufacturing processes. Sustainable biomaterials should be fabricated using energy-

* Corresponding author.
E-mail address: n.e.putra@tudelft.nl (N.E. Putra).

https://doi.org/10.1016/j.actbio.2025.06.051
Received 3 March 2025; Received in revised form 27 May 2025; Accepted 25 June 2025
Available online 26 June 2025

efficient technologies that use the smallest amounts of starting materials, and facilitate the use of recycled or renewable raw materials [1]. The leading technology that satisfies these requirements is additive manufacturing (AM) [2].

AM plays an important role in driving the transition towards more sustainable fabrication processes across various industries, including healthcare [2–4]. AM offers improved resource efficiency and on-demand manufacturing capabilities, thus reducing the requirements for inventory and transportation [5]. The integration of AM with artificial intelligence, *e.g.*, generative design, can enhance the optimization process for biomaterials [6,7], thereby reducing the energy intensiveness of manufacturing.

In addition to addressing environmental concerns, AM for healthcare should aim to improve patients' quality of life. Over the past decade, AM techniques have been extensively explored for the fabrication of biomaterials for tissue engineering, implants, and medical instruments [8,9]. Selecting an AM technique suitable for tailoring biomaterials, *e.g.*, for bone substitutes, is of importance [10,11]. It can improve treatment outcomes and reduce the need for outpatient care, thereby lowering the financial burdens [12].

The success of bone-substituting biomaterials hinges on several requirements [13–15]. An ideal biomaterial should exhibit (*i*) adequate interconnected porosity for nutrient transport and cell migration, (*ii*) mechanical properties that closely match those of the surrounding host tissue to ensure structural integrity and bone-preserving distribution of mechanical loads, (*iii*) osteogenic and angiogenic properties to promote bone tissue regeneration, (*iv*) a favorable immune response, (*v*) antimicrobial properties to prevent implant-associated infections, and (*vi*) biodegradability to allow for native tissue replacement over time [14]. AM technologies, such as selective laser melting (SLM) and direct ink writing (DIW), have been employed to develop biodegradable bone substitutes based on metals [16–20]. Specifically, iron (Fe)-based bone substitutes have been optimized using AM to meet the *in vitro* criteria of bone-substituting biomaterials [21] and have shown promising *in vivo* outcomes [22–24].

AM Fe-based bone substitutes feature controlled pore structure and geometry [25]. Furthermore, AM enables the *in situ* alloying of Fe with manganese (Mn) [26–28] and the incorporation of a bioceramic phase into the Fe matrix [21,29–32] to accelerate biodegradation rate, create paramagnetic behavior for magnetic resonance safety, and enhance bioactivity for bone tissue regeneration. As research progresses toward the clinical applications of Fe-based biomaterials, it is now crucial to focus on developing AM Fe-based bone substitutes that meet both performance and sustainability criteria. This parallel focus is essential for accelerating the sustainable development of such biomaterials, considering the extensive regulatory landscape governing medical device approval for patient treatment [33,34].

Biodegradable implants are preferred over permanent metallic implants for certain clinical cases. While the currently developed biodegradable implants are not considered sustainable regarding reusability or recyclability, they contribute to sustainability by eliminating the need for implant removal surgery. In the U.S. alone, millions of orthopedic procedures are performed every year, generating over 100,000 tons of medical waste [35]. The National Health Service in the UK produces more than 500,000 tons of waste and emits 25 megatons of CO_2 annually [36]. Biodegradable bone substitutes that eliminate a second surgical procedure can therefore contribute toward reducing both clinical wastes and the overall carbon footprint of healthcare.

Fe is an abundant element. Fe's extraction and recycling processes have been extensively investigated, with ongoing efforts focused on enhancing their environmental sustainability [37–39]. Moreover, the sustainability of AM Fe-based bone substitutes can be improved by replacing chemically synthesized bioceramics with recycled bioactive materials. Eggshells are a natural source of calcium carbonate ($CaCO_3$) [40]. Approximately 250,000 tons of eggshell waste are generated annually by the food-processing industry worldwide, and most of it is disposed of in landfills, causing pollution [41]. Utilizing waste-derived $CaCO_3$ from eggshells avoids mining virgin resources like apatite precursors [42].

Several studies have reported that eggshell powder enhances the osteogenic properties of hydrogel-based biomaterials, supporting new bone tissue regeneration *in vitro* and *in vivo* [43,44]. Moreover, eggshell powder has been successfully transformed into various calcium phosphate (CaP) bioceramics, such as hydroxyapatite (HAp), β-tricalcium phosphate (β-TCP), and brushite [45,46], offering a promising route for the development of sustainable bone substitutes.

In this study, we demonstrate DIW of biodegradable porous Fe scaffolds incorporating eggshell particles. This study marks the first use of waste-derived bioactive materials in the AM of metal matrix composites for application as bone-substituting biomaterials. We comprehensively evaluated the morphology, phase composition, and chemical composition of the composite scaffolds, as well as their *in vitro* biodegradation behavior, electrochemical responses, and changes in their mechanical properties along with biodegradation. Furthermore, the cytocompatibility and osteogenic potential of the composite scaffolds towards preosteoblasts (MC3T3-E1), and the antibacterial activity against methicillin-sensitive *Staphylococcus aureus* (MSSA) JAR 060131 and multidrug-resistant *S. aureus* (MDR-SA) LUH14616 were assessed.

2. Materials and methods

2.1. Preparation of Fe-eggshell ink

Fe powder (with 99.88 wt% purity, spherical particle shape, and particle sizes < 63 μm) was purchased from Material Technology Innovations Co. Ltd., China (Fig. 1**a**). Chicken eggs were purchased from a local supermarket in the Netherlands. The raw eggshells were cleaned with tap water, dried, ground, and sieved to obtain a batch of eggshell powder with particle sizes < 45 μm (Figure 1**b**). A powder mixture containing 80 vol% Fe and 20 vol% eggshell powder particles was blended with a 5 wt% hydroxypropyl methylcellulose binder (hypromellose, M_w ~86 kDa; Sigma Aldrich, Germany) prepared in water-ethanol solvent [28], hereafter denoted as Fe-eggshell ink. The volume percent of the powder in the ink was 47.45 %.

The flow rate of the ink (Q in mm^3/s) was calculated by dividing the volume of the extruded ink (mm^3) by time (s) and the rheological characteristics of the ink were evaluated using an MCR302 rheometer (Anton Paar GmbH, Germany).

2.2. Direct ink writing, debinding, and sintering

Porous cylindrical specimens (ϕ = 10 mm, h = 10.5 mm, Fig. 1**c**) were fabricated using the DIW technique with a 3D BioScaffolder 3.2 printer (GeSiM Bioinstruments and Microfluidics, Germany). The porous cylinders were constructed layer by layer according to a pattern design with a strut size of 410 μm and a macro-pore spacing (*i.e.*, distance between the strut) of 400 μm. The pattern orientation of each layer changed by 90° relative to the previous layer. The Fe-eggshell ink was extruded under a pressure of 250 kPa and at a printing speed of 3.5 mm/s. The as-printed specimens had a nominal relative porosity of 50 % and a nominal surface area of 40.4 cm^2. After DIW, the specimens were post-processed in a tube furnace (STF16/180 Carbonite Gero Ltd., UK) under flowing argon gas (grade 6.0, 99.9999 % purity). The debinding process was conducted at 350 °C for 1 h, followed by sintering at 1200°C for 6 h. The sintered specimens, hereafter referred to as Fe-CaO composite scaffolds, were cleaned in isopropyl alcohol for 15 min prior to further characterization. Porous specimens with smaller dimensions were fabricated for cell and bacterial culture experiments.

2.3. Characterization of microstructure, porosity, and phase composition

The shrinkage of the cylindrical specimens in diameter and height

Fig. 1. The morphologies of the (a) Fe and (b) eggshell powders. (c) A schematic illustration of direct ink writing (DIW) of the Fe-eggshell ink and the cylindrical porous scaffold design.

after post-processing was measured. The morphology, chemical composition, and characteristics of the struts (*i.e.*, strut diameter and macro-pore spacing) were inspected and measured using a scanning electron microscope (SEM; JSM-IT100, JEOL Ltd., Japan) and energy dispersive X-ray spectroscopy (EDS; JSM-IT100). The cross-section of the composite specimens was observed using SEM and the chemical composition was determined using EDS line and map analyses (JEOL JSM-IT100).

The morphologies of the struts and the cross-sections were visualized using micro-computed tomography (µCT; CoreTOM, TESCAN, Czech Republic). µCT images were acquired at a tube voltage of 120 kV and a tube current of 125 µA, with a resolution of 6 µm. The scan was performed in a 360° rotation for 23 min. The 16-bit µCT images were reconstructed using the 3D Slicer© software (v5.2.2, USA). To distinguish Fe and CaO in the composite specimens, a geometrically similar pure Fe scaffold was scanned to determine the threshold values of pure Fe. Image analysis was conducted using ImageJ (v1.54, NIH, USA). The porosity value of the Fe-CaO composite specimens was calculated using the BoneJ 7.0.17 plugin [47] in ImageJ.

The phase compositions of the raw eggshell powder and the Fe-CaO composite scaffold specimens were determined using an X-ray diffractometer (XRD; D8 Advance, Bruker, USA) in a Bragg-Brentano geometry and equipped with a LynxEye position-sensitive detector. The XRD measurement utilized Cu Kα radiation at 45 kV and 40 mA, spanning a scan range from 5° to 110° at a step size of 0.04° and a counting time of 2 s per step. The XRD results were analyzed using Diffrac Suite.EVA (v6.1, Bruker, USA).

The total and interconnected porosities of the Fe-CaO composite specimens were determined by weighing and using the oil-impregnation technique according to the ASTM standard B963-13 [48]:

$$\varphi_t = \left(1 - \frac{m/\rho_{Fe-CaO}}{V_{bulk}}\right) \times 100\% \quad (1)$$

$$\varphi_i = \left(\frac{\rho_{ethanol}}{\rho_{oil}} \times \frac{m_o - m_a}{m_o - m_{eo}}\right) \times 100\% \quad (2)$$

where φ_t and φ_i are the total and interconnected porosities [%], respectively, m is the mass [g] of the porous Fe-CaO composite specimen, ρ_{Fe-CaO} is the theoretical density of the Fe-CaO composite (*i.e.*, 7.42 g/cm^3), V_{bulk} is the bulk volume of the cylinder [cm^3], $\rho_{ethanol}$ and ρ_{oil} are the densities of ethanol and oil (*i.e.*, 0.789 g/cm^3 and 0.919 g/cm^3, respectively), m_a is the mass of the specimen in air [g], while m_o and m_{eo} are the masses of the oil-impregnated scaffolds in air and in ethanol [g], respectively.

2.4. In vitro biodegradation tests

2.4.1. Static immersion

The immersion tests of the Fe-CaO composite specimens were conducted over periods of 1, 4, 7, 14, and 28 days in the revised-simulated body fluid (r-SBF), which mimics the concentrations of the ions in human blood plasma [49] with an initial pH value of 7.40. The r-SBF volume was set at 6.7 mL for every cm^2 of the specimen's surface area (design value) [50]. The tests were performed at a temperature of 37 ± 0.5 °C, with a relative humidity of 95 %, and in an atmosphere containing 5 % CO_2. The composite specimens (in triplicate for each time point) were sterilized and the r-SBF medium was filtered through a pore size of 0.22 µm (Merck Millipore, Germany). At the designated time points, the specimens were retrieved for further characterization.

The concentrations of Fe^{2+}, Ca^{2+}, and PO_4^{3-} ions in r-SBF at various time points were measured using inductively coupled plasma-optical emission spectrometry (ICP-OES; iCAP 6500 Duo, Thermo Scientific, USA). The pH value of the medium was monitored using a pH electrode (InLab Expert Pro-ISM, METTLER TOLEDO, Switzerland). In addition to the global pH, to measure the initial elevated local pH surrounding the struts, the specimens were immersed in r-SBF with a 10 times lower volume ratio to specimen surface area (*i.e.*, 0.67 mL/cm^2). The local pH values were measured at selected time points.

2.4.2. Biodegradation products and corrosion rate

The phases in the biodegradation products at the top and lateral surfaces of the cylindrical specimens were identified using XRD. The morphologies of the biodegradation products at the periphery and the center of the specimens were inspected using SEM and their chemical compositions were determined using EDS. To determine the mass loss values, the biodegradation products from the retrieved specimens were removed using a solution containing HCl and 3.5 g/L hexamethylenetetramine (Sigma Aldrich, Germany), following the ASTM standard G1-03 [51]. The cleaning cycle was described in our previous publications [32,52].

The mass loss value was determined and the corrosion rate (*CR*) was calculated based on the ASTM standard G31-72 [53]:

$$CR_{immersion} = 8.76 \times 10^4 \times \frac{m}{A \times t \times \rho} \quad (3)$$

where $CR_{immersion}$ is the corrosion rate [mm/year], m is the mass loss value [g], A is the surface area of the composite specimen [cm^2] calculated based on the initial scaffold design value, t is the immersion period [h], and ρ is the theoretical density of the Fe-CaO composite [g/cm^3].

The composite specimens, retrieved after 28 days of immersion, were scanned using µCT. The images were reconstructed, and the segmented volume of the retrieved specimens was compared to the initial volume of the specimens in ImageJ. The volume loss attributed to biodegradation was calculated using the BoneJ 7.0.17 plugin [47] in ImageJ.

2.4.3. Electrochemical measurements

The electrochemical responses of the Fe-CaO composite specimens during immersion in r-SBF were measured using a potentiostat (SP-200, Bio-Logic Science Instruments, France). The setup consisted of a saturated calomel reference electrode, a counter electrode made of graphite, and a specimen partially embedded in an acrylic resin as the working

electrode. The initial pH of r-SBF medium was 7.40. The temperature was maintained at 37 ± 0.5 °C during the measurements. The exposed surface area of the specimens was calculated based on their initial design. Electrochemical impedance spectroscopy (EIS) was performed at frequencies ranging between 100 kHz and 10 mHz using a 10 mV sine amplitude *vs.* open circuit potential (OCP). Linear polarization resistance (LPR) was measured at a scanning rate of 0.167 mV/s from -25 to +25 mV *vs.* OCP. The electrochemical tests were conducted for up to 28 days.

2.5. Mechanical tests

2.5.1. Uniaxial compression tests

The compressive mechanical properties of the Fe-CaO composite specimens before and after the *in vitro* biodegradation tests were evaluated according to the ISO standard 13314:2011 [54]. The compression tests were carried out using a universal mechanical testing machine equipped with a 100 kN load cell (Zwick Z100, Germany) at a crosshead speed of 3 mm/min. The 0.2 % offset compressive stress (referred to as the yield strength) and the quasi-elastic gradient (hereafter referred to as the elastic modulus) were determined from the stress-strain curves. The stress was calculated as force divided by initial cross-sectional area, and the strain was calculated as the ratio of displacement to the initial length of the cylindrical specimens. The yield strength was identified as the stress value at the intersection of the stress-strain curve with the 0.2 % offset line, which is parallel to the initial linear region of the stress-strain curve. The elastic modulus was defined as the slope of the initial linear region of the stress-strain curve.

2.5.2. Fatigue tests in air and r-SBF

The compressive fatigue properties of the Fe-CaO composite were evaluated under compression-compression cyclic loading in air and in r-SBF using a dynamic mechanical testing machine (Instron E10000 ElectroPuls with a 10 kN load cell) equipped with an in-house fabricated double-wall chamber. Four maximum stress levels (*i.e.*, $0.6\sigma_y$, $0.7\sigma_y$, $0.8\sigma_y$, and $0.9\sigma_y$, where σ_y is the yield stress = 6 MPa) were applied at a frequency of 15 Hz. The minimum stress level was set at 0.1 times the corresponding maximum stress level.

During the biodegradation fatigue tests, the Fe-CaO composite specimens were immersed in 300 mL r-SBF inside the chamber, with the temperature maintained at 37 °C. A purging gas composed of 95 % N_2 and 5 % CO_2 was introduced into the chamber to increase the buffering capacity. For the fatigue tests under ambient atmospheric condition (in air), compression-compression cyclic loading was applied to the specimens using the same mechanical testing machine and setup, under three different maximum stresses (*i.e.*, $0.6\sigma_y$, $0.8\sigma_y$, and $0.9\sigma_y$) with the same loading ratio and loading frequency.

All the tests were ended either after 3 million cycles of loading (=55.6 h) or upon reaching strain of 5 % (indicating specimen failure) was reached. The tests were performed in triplicate at each stress level. The fatigue strength of the specimens was defined as the maximum stress that could be applied without causing specimen failure after 3 million loading cycles.

2.6. Cell tests for cytocompatibility and osteogenic potential

2.6.1. Preculture of preosteoblasts

Mouse preosteoblasts MC3T3-E1 (#acc210, DSMZ, Germany) were cultured in a flask in a cell culture incubator at a temperature of 37 ± 0.5 °C, with a relative humidity of 95 %, and in an atmosphere containing 5 % CO_2. The cell culture media (Thermo Fisher Scientific, USA) consisted of α-minimum essential medium (α-MEM) supplemented with 10 % fetal bovine serum (FBS) and 1 % penicillin/streptomycin. The composite specimens were conditioned in the cell culture media for 72 h prior to cell seeding and culture.

2.6.2. Cell culture on the composite specimens

Preosteoblasts (5×10^4 cells per specimen) were seeded on the conditioned composite specimens ($\phi = 6$ mm and $h = 1$ mm) and cultured in 8 mL of the cell culture media in a 6-well plate. From day 2 onwards, osteogenic cell culture medium with the supplements of 1:1000 ascorbic acid and 1:500 β-glycerophosphate was used.

The specimens (in triplicate for each time point) were cultured for up to 21 days. The viability of the cells residing on the specimens was determined using LIVE/DEAD™ viability/cytotoxicity kit (Thermo Fisher Scientific, USA) at days 1, 4, 7, and 14, following the procedure described in our previous publications [20]. The morphology of the preosteoblasts on the specimens at days 7, 14, and 28, was observed using SEM (JSM-IT100).

2.6.3. Staining of cell nuclei and osteogenic markers

After cell culture, the specimens were washed with phosphate buffer saline (PBS), fixed using 4 % paraformaldehyde at room temperature for 15 min, and then permeabilized with 0.5 % Triton in PBS at 4°C for 5 min (Sigma Aldrich, Germany). The specimens retrieved on day 7 were stained with 4′,6-diamidino-2-phenylindole (DAPI; 1: 1000 per specimen, Thermo Fisher Scientific, USA) to visualize the cell nuclei. The specimens retrieved on days 14 and 21 were immunostained for the osteogenic markers Runt-related transcription factor 2 (RUNX2, ab192256, Abcam, UK) and osteopontin (OPN, sc21742, Santa Cruz Biotechnology, USA). Therefore, after fixation and permeabilization, the specimens were incubated in well-plates containing 1 % bovine serum albumin (BSA) in PBS at 37 °C for 5 min. Primary antibodies, including anti-Runx2 anti-rabbit (1:250 per specimen, Abcam, UK) and anti-OPN anti-mouse (1:100 per specimen, Santa Cruz Biotechnology, USA) were added, followed by incubation at 37 °C for 1 h. Subsequently, the specimens were washed using 0.5 % Tween in PBS (Sigma Aldrich, Germany) and incubated at 37 °C for 1 h in 1 % BSA in PBS with conjugated secondary antibodies Alexa Fluor 594 anti-rabbit (1:100, Thermo Fischer Scientific, USA) and Alexa Fluor 488 anti-mouse (1:200, Thermo Fischer Scientific, USA). The specimens were washed using 0.5 % Tween in PBS. Finally, the specimens were visualized using a fluorescent microscope (ZOE cell imager, Bio-Rad, USA).

2.6.4. Reverse transcription-quantitative polymerase chain reaction (RT-qPCR)

The gene expression of MC3T3-E1 cells was assessed at days 7, 14, and 21 (in triplicate per time point) for the osteogenic markers RUNX2, alkaline phosphatase (ALP), OPN, and osteocalcin (OCN). The cells cultured on geometrically similar Ti6Al4V specimens served as the control group. Ubiquitin C (UBC) was selected as the reference gene. At each time point, ribonucleic acid (RNA) was isolated with the RNeasy micro kit (Qiagen, Germany). Then, the RNA was converted to complementary deoxyribonucleic acid (cDNA) using a Quantitect Reverse Transcription kit (Qiagen, Germany). RT-qPCR was conducted on the Rotor X gene PCR system and the Quantinova SYBR Green PCR kit (Qiagen, Germany), with 5 ng cDNA for each measurement. The delta threshold cycle (CT) and delta delta CT values were calculated and the fold change in each gene expression was reported relative to that observed on the Ti6Al4V specimens.

2.7. Antibacterial tests

2.7.1. Bacterial strains and culture

The methicillin-sensitive *S. aureus* (MSSA) JAR060131, obtained from a patient with an orthopedic device-related infection [55,56], and the multidrug-resistant *S. aureus* (MDR-SA) LUH14616 clinical isolates [57] were used in the present study. Prior to each experiment, bacteria from frozen stocks were grown overnight at 37 °C on Luria-Bertani (LB) agar plates (Roth, Germany).

Overnight cultures were prepared by resuspending a single colony into 5 mL tryptic soy broth (TSB; BD, USA), followed by incubation for

18 h at 37 °C and 180 rpm. For the bactericidal assay, the bacteria were cultured to mid-logarithmic growth phase at 37 °C and 180 rpm, and diluted in Roswell Park Memorial Institute (RPMI) 1640 medium (Sigma Aldrich, Germany) to 1×10^6 colony-forming units (CFU)/mL based on the optical density of the suspension at 600 nm.

2.7.2. Bactericidal assay

The composite and glass (control) specimens ($\phi = 6$ mm and $h = 1$ mm) were placed in a 48-well plate and 85 μL of the freshly prepared bacterial inoculum suspension was added on top of the specimens, *i.e.*, 8.5×10^4 CFU per specimen, based on the JIS Z2801:2000 [58]. Subsequently, 200 μL RPMI was added, fully submersing the specimens (total volume was 285 μL), and incubated at 37 °C and 100 rpm. After 4 h, the specimens were removed from the RPMI culture medium and washed in PBS. The specimens were then ultrasonicated for 30 s and vortexed for 30 s (three times), to detach the adherent bacteria. The resulting sonicates and the RPMI medium were 10-fold serially diluted and 5 μL was plated in 5-fold on LB agar, incubated overnight at 37 °C, and the following day, the number of bacteria adherent to the specimen and present in the medium, respectively, was determined. For both strains, three specimens per group were tested in three separate experiments (*i.e.*, a total of $n = 9$ specimens per group). The bactericidal activity of the composite specimens was also compared with that of geometrically similar pure Fe specimens [20].

2.7.3. Bacterial permeabilization assay

Eluates from Fe-CaO composite and Fe (control) scaffolds ($\phi = 6$ mm and $h = 1$ mm) were prepared by immersing the specimens in 1.5 mL RPMI within 50 mL Falcon tubes and incubating them at 37 °C with shaking at 120 rpm for 4 h. MSSA and MDR-SAA bacterial suspensions (5×10^7 CFU, mid-log phase) were prepared in 500 μL volumes in Eppendorf tubes. The suspensions were centrifuged at 13,000 rpm for 5 min at RT, and the supernatants were discarded to obtain bacteria pellets. The bacterial pellets were each exposed to 500 μL of scaffold eluates ($n = 3$ per group) and incubated at 37 °C for 5 min. Following exposure, the suspensions were centrifuged again, and the supernatants were discarded.

Next, 200 μL of 100 μM propidium iodide (PI) solution was added to the bacterial pellets, and samples were incubated at RT in the dark for 15 min. After staining, the samples were centrifuged at 13,000 rpm for 5 min at RT, and the supernatants were removed. The stained bacterial pellets were resuspended in 200 μL PBS and transferred to a well plate for measurement. Fluorescence measurements were conducted using an excitation wavelength of 488 nm, scanning emission from 500 to 800 nm. The fluorescence peak at 617 nm was used to indicate bacterial membrane permeabilization.

2.7.4. CDC biofilm reactor (CBR)

The composite and porous Ti6Al4V (control) specimens ($\phi = 10$ mm and $h = 2.5$ mm) were placed in holders of the CDC biofilm reactor (CBR90, BioSurface Technologies Corporation, USA), containing 400 mL of RPMI medium supplemented with 1 % (v/v) TSB. Subsequently, the medium was inoculated with 1 mL overnight culture (containing ~1×10^8 CFU/mL) to reach a final concentration of 2.5×10^5 CFU/mL of either MSSA or MDR-SA. After 4 h culture at 37°C and a baffle rotation speed of 120 rpm, the specimens were retrieved, washed in PBS, and the number of adherent bacteria was determined as described above. For both strains, two specimens per group were tested in three separate experiments (*i.e.*, a total of $n = 6$ specimens per group). The morphology of bacteria on the specimen scaffolds was observed using SEM (JSM-IT100).

2.8. Statistical analysis

All statistical analyses were performed using GraphPad Prism (GraphPad Software Inc., USA). The statistical analysis of qPCR results was performed using a one-way ANOVA, followed by a Tukey multiple comparison *post hoc* test. The CFU counts data did not pass the Shapiro-Wilk test for normality. Therefore, the statistical analysis of CFU counts for two-sample comparisons was performed using non-parametric two-tailed Mann-Whitney rank sum test.

3. Results

3.1. Morphologies and chemical compositions of the porous Fe-CaO composite scaffolds

The AM of the scaffold specimens from the composite ink containing Fe and 20 vol% eggshell powder was achieved using the DIW technique. The Fe-eggshell ink exhibited a flow rate of 6.33 ± 0.07 mm^3/s. Cylindrical green-body specimens were constructed as designed with the layer turned 90° at every other layer (Fig. 2**a**). The green-body struts were composed of spherical Fe particles and irregular eggshell particles, bonded by the hypromellose binder (Fig. 2**b-c**). After DIW, the cylindrical green-body scaffolds were dried under ambient room conditions for 30 min and transferred to a crucible for post-AM heat treatment, without causing any visible deformation. After debinding and sintering, the cylindrical specimens retained their initial geometrical shape, with shrinkages of 3.4 ± 0.6 % in height and 4.6 ± 0.4 % in diameter. The strut diameter and macro-pore spacing of the composite scaffolds were 408 ± 2 μm and 354 ± 3 μm, respectively. An open micro porous architecture inside the struts was created during sintering (Fig. 2**d-f**). At a higher magnification (Fig. 2**f**), the powder particles were shown to be fused together. The irregularly shaped particles (Fig. 2**f**) were rich in Ca (see the results of EDS spot analysis at points 1 and 2, Table 1).

The decomposition of the eggshell powder started around 650°C (**Figure S1**). During sintering, the main component of the eggshell, $CaCO_3$ (Fig. 2**g**) transformed into the CaO phase, resulting in the composite specimens primarily composed of the α-Fe and CaO phases (Fig. 2**h**). The $Ca_2Fe_2O_5$ phase with low intensities, corresponding to a low concentration, was detected by XRD (*i.e.*, ~ 1-2 wt%, Fig. 2**h**). Theoretically, the decomposition of 20 vol% eggshell $CaCO_3$ (M_w= 100.087 g/mol, ρ = 2.71 g/cm^3) in the specimens results in the Fe-CaO composite scaffolds containing 9 vol% CaO phase (M_w= 56.077 g/mol, ρ = 3.34 g/cm^3). Overall, the post-AM debinding and sintering reduced the mass of the composite specimens by 4.9 ± 0.1 %, which was due to the evaporation of binder and the phase conversion of eggshell $CaCO_3$ into CaO.

The total porosity values of the porous Fe-CaO specimens were 70 ± 1 % (calculated by weighing) and 69 ± 1 % (calculated by μCT). The interconnected porosity value of the specimens was 68 ± 1 % (calculated by using the oil-impregnation method). The μCT image reconstruction enabled the visualization of the porous architecture on the cross-sections of the struts (Fig. 2**i-j**). The micro porosity within the struts, calculated by μCT, was 21 ± 2 %. EDS mapping analysis on the cross-section of the specimen revealed an aggregated distribution of Ca in the α-Fe matrix (Fig. 3**a**). Furthermore, EDS line analysis indicated that Fe diffused into CaO particles with a penetration depth of at least 9.7 μm (Fig. 3**b**).

3.2. Biodegradation behavior

3.2.1. Biodegradation rate and ion release from in vitro immersion tests

White and yellow-brown colored biodegradation products were observed on the composite specimens after immersion tests in r-SBF at various time points (Fig. 4**a**). The yellow-brown products appeared on both the top and lateral surfaces of the cylinders, whereas the white products accumulated on the lateral surface of the specimens. As a result of biodegradation, the mass of the specimens decreased. The cumulative mass loss was 6 ± 2 % on day 4, which increased to 9 ± 3 % on day 7, 13 ± 2 % on day 14, and 15 ± 1 % on day 28 (Fig. 4**b**). The mass loss value at day 28 corresponded to a biodegradation rate of 0.107 ± 0.003 mm/

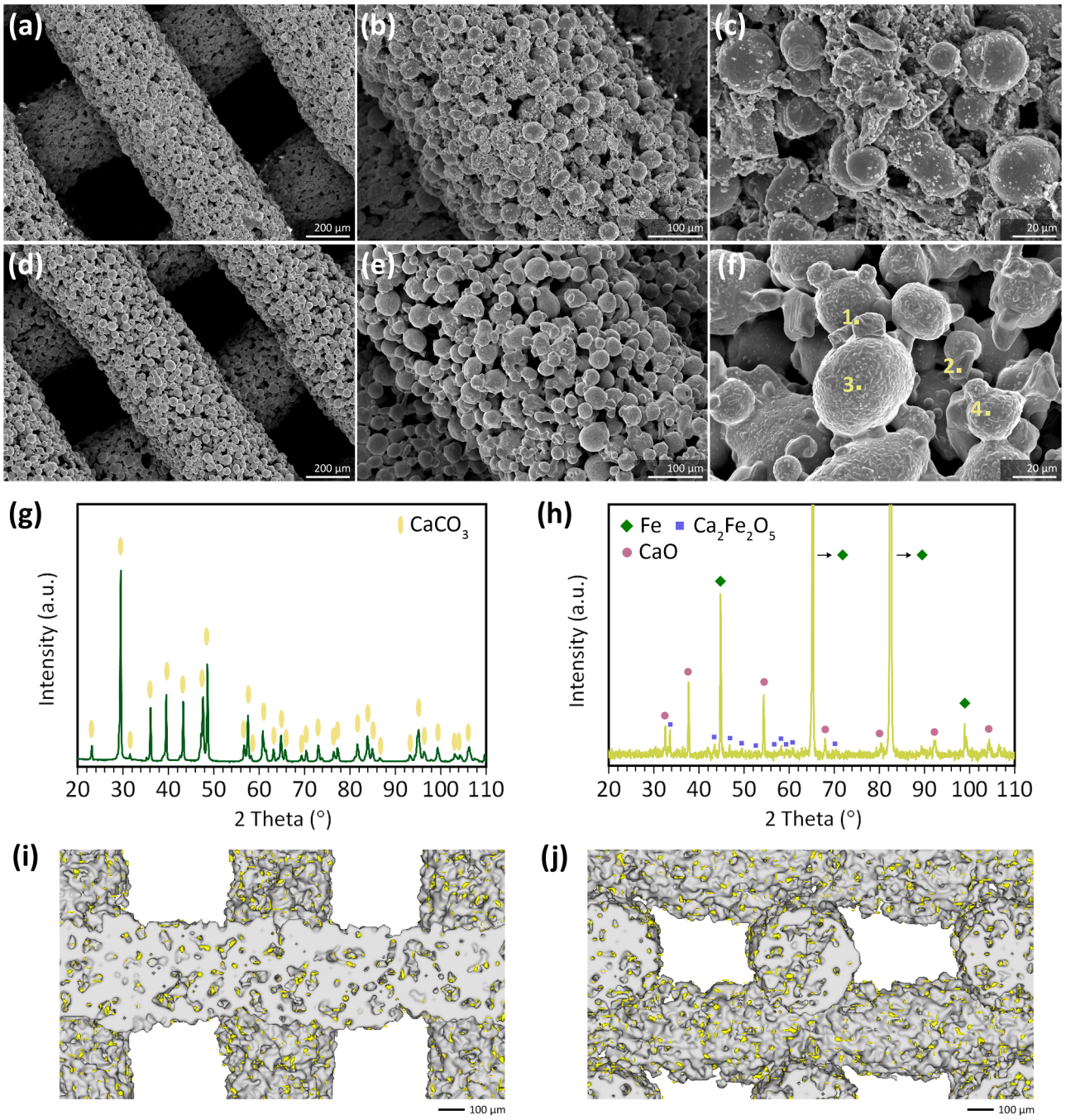

Fig. 2. The morphologies of the green-body (a) Fe-eggshell specimens, (b) their struts, and (c) powder particles bonded by the hypromellose binder. The morphologies of the sintered (d) porous Fe-CaO composite specimens, (e) their struts, and (f) sintered powder particles. The number with a dot sign indicates the location of the EDS spot measurement. The phase compositions of the (g) raw eggshell powder and (h) Fe-CaO specimens. (i, j) The cross-sections of the composite specimens as visualized by µCT.

Table 1
The chemical compositions of the porous Fe-CaO composite specimens (wt%), as determined by EDS spot analysis (shown in Figure 2f, with an accuracy of ±2%).

	EDS point	C	O	Ca	Fe
Fe-CaO	**1**	11.81	28.62	46.51	13.05
	2	5.55	9.15	60.43	24.87
	3	11.88	10.07	23.36	54.69
	4	8.04	1.61	1.51	88.84

year.

During biodegradation, the composite specimens released Fe^{2+} and Ca^{2+} ions (Fig. 4**c-d**). The concentration of Fe^{2+} ions in r-SBF increased from 0.02 ± 0.01 mg/L at day 1 to 0.08 ± 0.01 mg/L on day 4, then decreased to 0.03 ± 0.01 mg/L on day 7, 0.04 ± 0.01 mg/L on day 14, and 0.03 ± 0.01 mg/L on day 28 (Fig. 4**c**). The concentration of Ca^{2+} ions exceeded the initial concentration in r-SBF at all the tested time points, with the highest value observed on day 4. The concentration of Ca^{2+} ions increased from 122.1 ± 0.4 mg/L on day 1 to 167 ± 2 mg/L on day 4, then decreased to 140.2 ± 0.3 mg/L on day 7, to 127 ± 1 mg/L on day 14, and to 115 ± 1 mg/L on day 28 (Fig. 4**d**). The concentration of PO_4^{3-} ions in r-SBF decreased from 96 ± 1 mg/L on day 1 to 17.78 ± 0.07

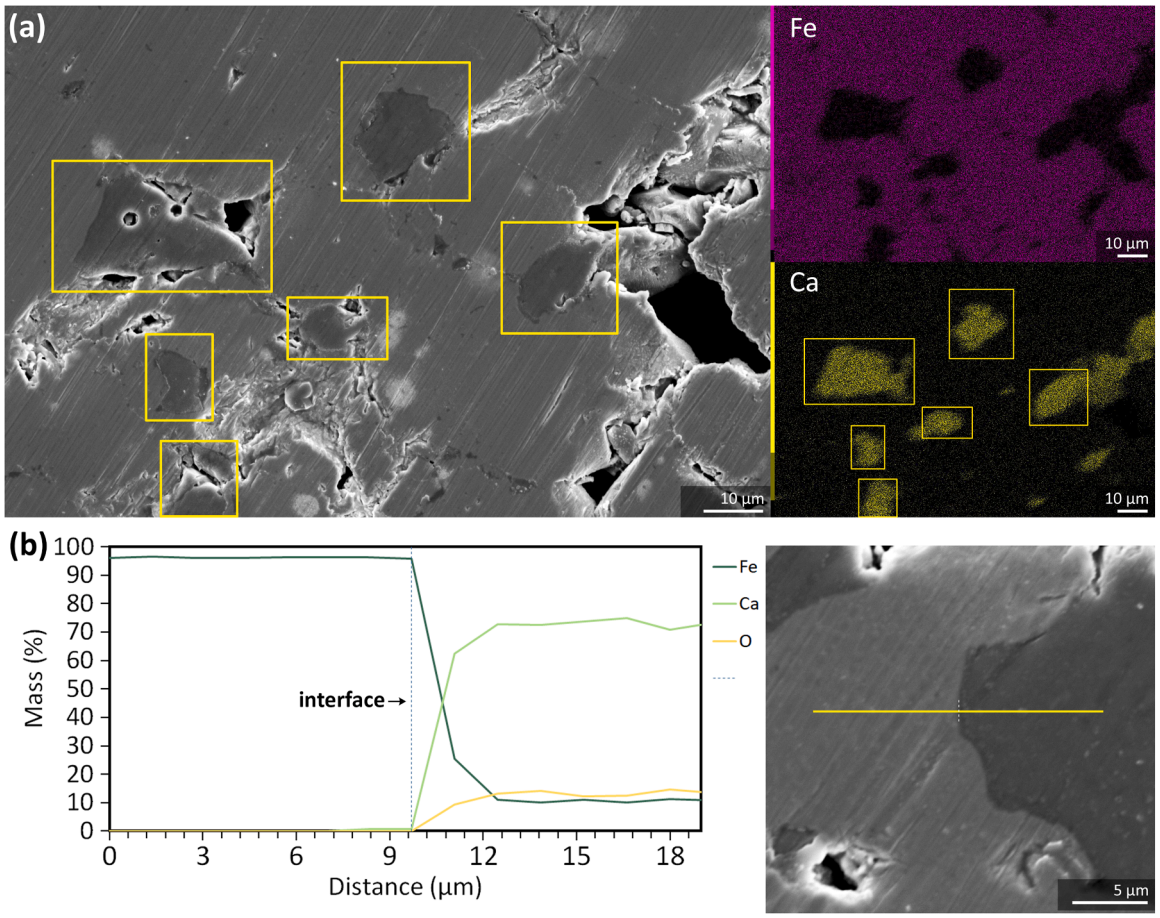

Fig. 3. The cross-sections of the Fe-CaO composite specimens as visualized by SEM with (a) EDS mapping analysis and (b) EDS line analysis across the interface of the Fe and CaO phases.

mg/L on day 28 (Fig. 4**e**).

The global pH value of r-SBF reached 7.56–7.60 over the immersion tests. The global pH value was relatively stable as compared to the initial pH of r-SBF (*i.e.*, 7.40), which is likely due to the immersion tests being conducted in a 5% CO_2 environment. However, the local pH value was elevated (Fig. 4**f**). The local pH was 7.80 ± 0.04 after 4 h of immersion, and elevated to 8.1 ± 0.1 after 18 h of immersion. The value slightly decreased to 7.88 ± 0.06 on day 1, 7.7 ± 0.1 on day 2, and stabilized to 7.55 ± 0.03 on day 7 (Fig. 4**f**).

3.2.2. *Electrochemical responses during immersion tests*

The electrochemical response of the porous Fe-CaO composite specimens was evaluated during immersion in r-SBF. The OCP values started at -679 ± 66 mV on day 1, increased to -559 ± 67 mV on day 4, and fluctuated around -549 ± 49 mV on day 7, -535 ± 23 mV on day 14, and -544 ± 38 mV on day 28 (Fig. 4**g**). The polarization resistance (R_p) values of the composite specimen were initially 11 ± 1 kΩ cm^2 on day 1, increased to 20 ± 1 kΩ cm^2 on day 4, and maintained at 19 ± 3 kΩ cm^2 on day 7, 22 ± 2 kΩ cm^2 on day 14, and 20 ± 1 kΩ cm^2 on day 28 (Fig. 4**h**).

The impedance modulus values in the lower frequency region (*i.e.*, 0.01 Hz) were initially 8 ± 1 kΩ cm^2 on day 1, increased to 14 ± 1 kΩ cm^2 on day 4, and maintained at 14 ± 5 kΩ cm^2 on day 7, 15 ± 3 kΩ cm^2 on day 14, and 15 ± 2 kΩ cm^2 on day 28 (Fig. 4**i-j**). At higher frequencies (*i.e.*, the mid frequency region of 10 Hz), the Bode impedance modulus values were 1.5 ± 0.2 kΩ cm^2 on day 1, increased to 3.3 ± 0.3 kΩ cm^2 on day 4, and maintained at 3 ± 1 kΩ cm^2 on day 7 and day 14, and increased to 3.6 ± 0.5 kΩ cm^2 on day 28 (Fig. 4**i-j**). Moreover, the Nyquist impedance plots show a time constant at high frequencies, represented by a quarter-circle arc, which then extended into a horizontal line in the mid-frequency region, and concluded with an elevated trajectory as the lines approached the low-frequency region (Fig. 4**k**). The linear extrapolation line in the low frequency range (from 0.01 to 0.05 Hz) exhibited an angle of 40–43° relative to the *x*-axis for all exposure times.

3.2.3. *Characteristics and morphologies of the biodegradation products*

At the top surface of the cylindrical specimens, the γ-iron oxide hydroxide (γ-FeOOH) and $CaCO_3$ phases were detected at all time points (Fig. 5**a**), while the carbonatious HAp phase ($Ca_{3.89}Na_{0.09}Mg_{0.02}$)($Ca_{5.55}Na_{0.12}Mg_{0.03}$)$(PO_4)_{5.2}(CO_3)_{0.8}(OH)$ was only identified after 28 d of immersion. On the lateral surface of the specimens, the white biodegradation products were determined to be a combination of pure HAp ($(Ca_5(PO_4)_3(OH))$ and $CaCO_3$ (Fig. 5**b**). The SEM images revealed that the dense biodegradation products covered the struts at the top surface of the composite specimens (Fig. 6). These products progressively filled the peripheral macro-pore spacings at the top (Fig. 6**a-d**) and on the lateral surfaces of the specimens (Fig. 7**a-b**).

On day 7, the dense biodegradation products (Fig. 6**e**) contained 66–80 wt% Fe and up to 4.6 wt% Ca (Fig. 6**f**, Table 2). On day 14, the biodegradation products displayed a particulate morphology (Fig. 6**g**) with a reduced Fe concentration (*i.e.*, 40–44 wt%) and an increased Ca concentration (*i.e.*, 10–17 wt%, Fig. 6**h**, Table 2). After 28 days of immersion, more particulate products were observed (Fig. 6**i**). They were composed of 40–43 wt% Fe, Ca of a higher concentration (*i.e.*, 21–35 wt %) and the other elements (Fig. 6**j**, Table 2). On the other hand, the biodegradation products on the lateral surface of the specimens were rich in Ca. On day 1, the Ca concentration reached 48 wt% (Fig. 7**a**,

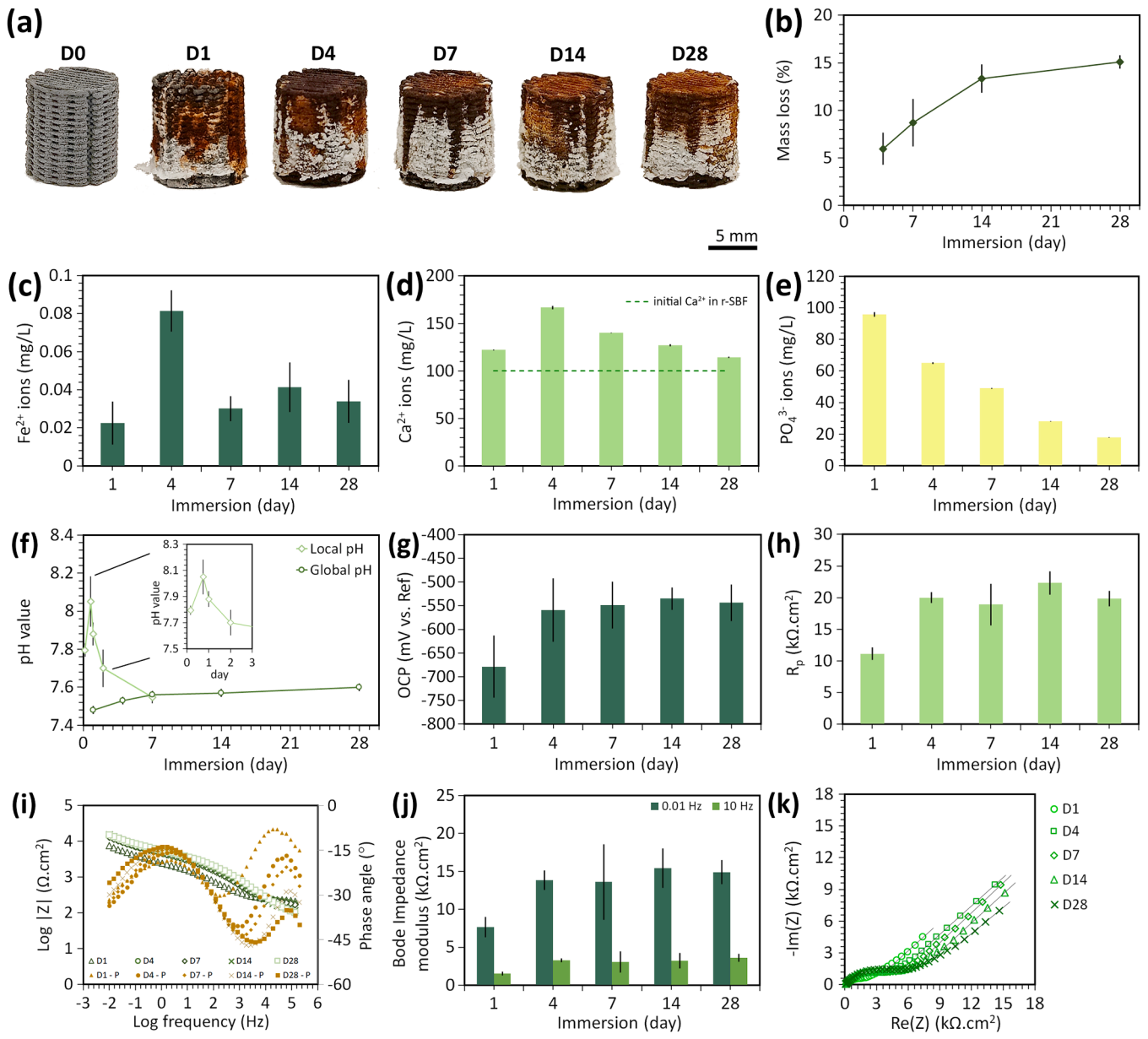

Fig. 4. The biodegradation and electrochemical characteristics of the porous Fe-CaO composite specimens: (a) The visual observation of the specimens before and after immersion at different time points. (b) Mass loss over time. The evolution of the (c) Fe^{2+}, (d) Ca^{2+}, and (e) PO_4^{3-} concentrations in the r-SBF medium over time. The electrochemical responses expressed as (f) OCP values, (g) R_p values from LPR measurements, (h) Bode impedance plots, (i) impedance modulus values in the low frequency region of 0.01 Hz and in the mid-frequency of 10 Hz, and (j) Nyquist impedance plots at selected exposure times. The bars represent the mean and the error bars indicate the standard deviation.

Table 2). On day 28, the Ca concentration increased to 56–74 % and P concentration of 8–18 % was detected (Fig. 7**b**, Table 2). Furthermore, the biodegradation products of the porous Fe-CaO composite scaffolds, formed during bacteria culture and cell culture, exhibited a similar elemental composition (*i.e.*, Fe, Ca, C, and O, **Table S1**) to that formed during biodegradation in r-SBF.

After 28 days of biodegradation, the micro porosity value within the struts became 4 ± 1% (calculated by μCT, Fig. 7**c-d**). Despite the dense corrosion products in the struts, the macro-pore spacings at the center of the specimens remained available (Fig. 7**c-d**). The original CaO particles were still detected as well (Fig. 7**e**). Based on μCT analysis, the composite specimens had a volume reduction of 12 ± 1 %.

3.3. Mechanical properties

The compressive stress-strain curves of the composite specimens exhibited linear elastic deformation at the start, followed by plastic deformation (Fig. 8**a**). The specimens had a yield strength of 6 ± 1 MPa and an elastic modulus of 0.36 ± 0.06 GPa. The yield strength value fluctuated because of biodegradation (*i.e.*, 5.3 ± 2 MPa on day 4, 5.1 ± 2 MPa on day 7, and 6.1 ± 0.8 MPa on day 14). After 28 days of immersion, the yield strength value decreased to 4.1 ± 0.6 MPa (Fig. 8**b**). Biodegradation also had an impact on the elastic modulus of the specimens (Fig. 8**c**). The elastic modulus values were 0.14 ± 0.05 GPa, 0.15 ± 0.03 GPa, 0.11 ± 0.03 GPa, and 0.14 ± 0.04 GPa, respectively, after 4, 7, 14, and 28 days of immersion.

The Fe-CaO composite specimens remained intact at the macro scale after cyclic loading in air and r-SBF (Fig. 8**e**). No buckling, distortions,

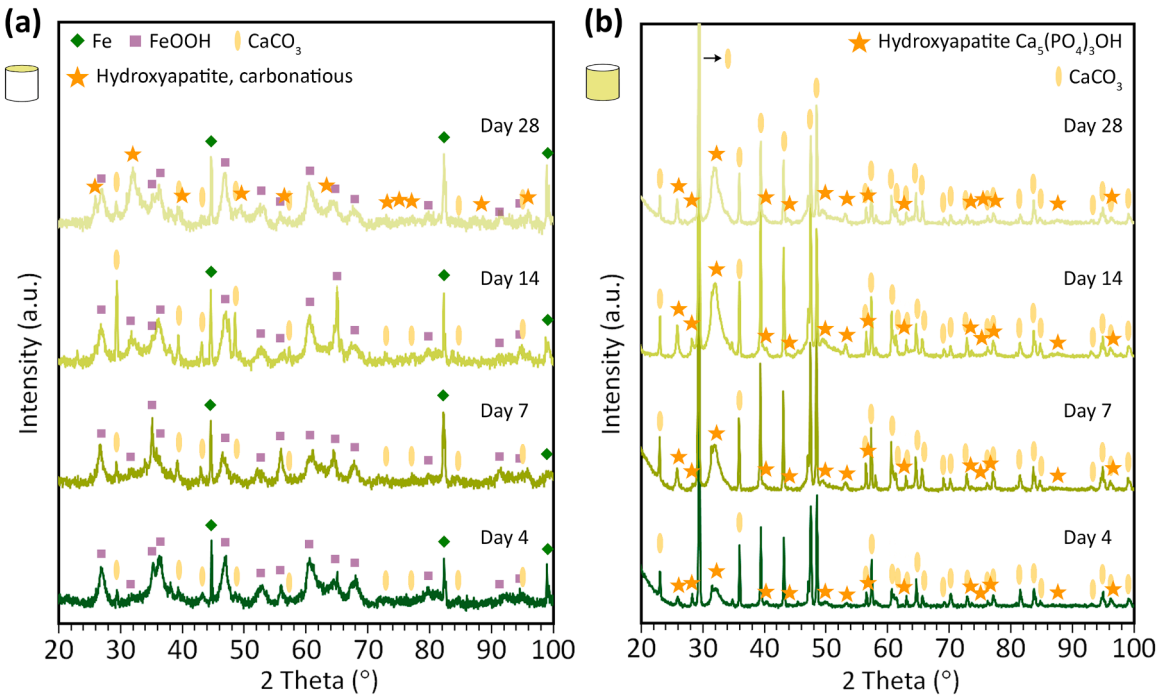

Fig. 5. The phase compositions (a) at the top surface and (b) at the lateral surface of the Fe-CaO composite specimens after *in vitro* immersion at different time points.

fracture plane, or slippage was observed in the specimens after cyclic loading with or without simultaneous biodegradation. In air, the specimens showed no visible changes, whereas those subjected to cyclic loading in r-SBF formed biodegradation products (Fig. 8**e**). The fatigue strength of the porous Fe-CaO composite specimens, at 3 million cycles, decreased from $0.9\sigma_y$ in air to $0.7\sigma_y$ in r-SBF (Fig. 8**f**). The specimens endured an average of 0.8 million cycles at $0.8\sigma_y$ in r-SBF and 0.3 million cycles at $0.9\sigma_y$ in r-SBF. As expected, cracks were found at the neck regions where the Fe powder fused with the eggshell-derived CaO particles in the specimens tested in air (Fig. 8**g**). For the specimens tested in r-SBF, the extensive coverage of biodegradation products on the struts surface obscured the visibility of cracks (Fig. 8**h**). However, we believe that cracks likely formed at the same neck regions, as these areas represent the weakest bonding sites of the metal and ceramic.

3.4. Antibacterial properties

The composite specimens exhibited bactericidal activities against the MSSA strain, with a 5.5-log and 4.2-log lower number of planktonic and adherent bacteria, respectively, when compared to the control substrates, resulting in full eradication of the bacteria (Fig. 9**a**). The bactericidal activities of the composite specimens were also observed against the MDR-SA strain with a 6-log lower number of planktonic bacteria, fully eradicating all bacteria, and a 3.9-log lower number of adherent bacteria in comparison to the control substrates (Fig. 9**b**).

Geometrically similar porous pure Fe scaffold showed no bactericidal effect, when compared to the glass control, so Fe itself has no antibacterial activity (**Figure S3**). When incubated in the CDC biofilm reactor for 4 h, the composite specimens had significantly less bacteria adhering, resulting in 3.4-log and 3.3-log lower numbers of adherent MSSA and MDR-SA, respectively, as compared to the geometrically similar porous Ti6Al4V specimens (Fig. 9**c-d**). Bacteria cultured on the porous Ti6Al4V specimens stacked on top of each other in several layers, producing a biofilm-like extracellular matrix (Fig. 9**e, g**). Meanwhile, the surface of the composite specimens showed a minimal presence of adherent bacteria (Fig. 9**f, h**).

3.5. In vitro cytocompatibility and osteogenic potential

3.5.1. Live-dead staining, osteogenic differentiation, and cell morphology

The fluorescent images revealed the viability of the preosteoblast MC3T3-E1 cells cultured on the porous composite specimens at different time points, *i.e.*, on day 1 (Fig. 10**a**), on day 4 (Fig. 10**b**), on day 7 (Fig. 10**c**), and on day 14 (Fig. 10**d**). On day 7, cell nuclei were observed to be homogeneously distributed on the struts of the specimens (Fig. 10**e**). The cells exhibited a spread morphology amidst the biodegradation products (Fig. 10**h**). On day 14, the cell osteogenic differentiation was indicated by the immunostaining of RUNX2 (Fig. 10**f**). On day 21, immunofluorescent OPN was detected, suggesting an initial phase of *in vitro* mineralization (Fig. 10**g**). The cell density increased over time, indicating cell proliferation (Fig. 10**h-j**). Moreover, cells aligned themselves along the struts (Fig. 10**i**) and produced extracellular matrix (Fig. 10**j**).

3.5.2. Osteogenic gene expression

The expression of osteogenic genes in the cells cultured on the composite specimens was compared to that on the porous Ti6Al4V specimens (Fig. 10**k-n**). The levels of RUNX2 and ALP on the composite specimens were comparable to those on the Ti6Al4V specimens on day 7 and were relatively lower on days 14 and 21 (Fig. 10**k-l**), with no statistical differences observed. On day 7, the OPN expression on the composite specimens was 1.5-fold higher than that on the Ti6Al4V specimens (Fig. 10**m**). At the same time point, the OCN levels were comparable (Fig. 10**n**). On day 14, the expressions of OPN and OCN on the composite specimens increased significantly (*i.e.*, 4.2 ± 0.6 fold, $p \leq 0.001$ and 11.5 ± 0.4 fold, $p < 0.0001$, respectively) as compared to those on the Ti6Al4V specimens (Fig. 10**m-n**). At a later time point (*i.e.*, day 21), the expressions of OPN and OCN remained higher in the composite specimens (*i.e.*, 3.6 ± 0.7 fold, $p \leq 0.001$, and 6.6 ± 0.3 fold, $p < 0.0001$) as compared to those in the Ti6Al4V specimens (Fig. 10**m-n**).

4. Discussion

Porous Fe scaffolds containing waste-derived eggshell particles were

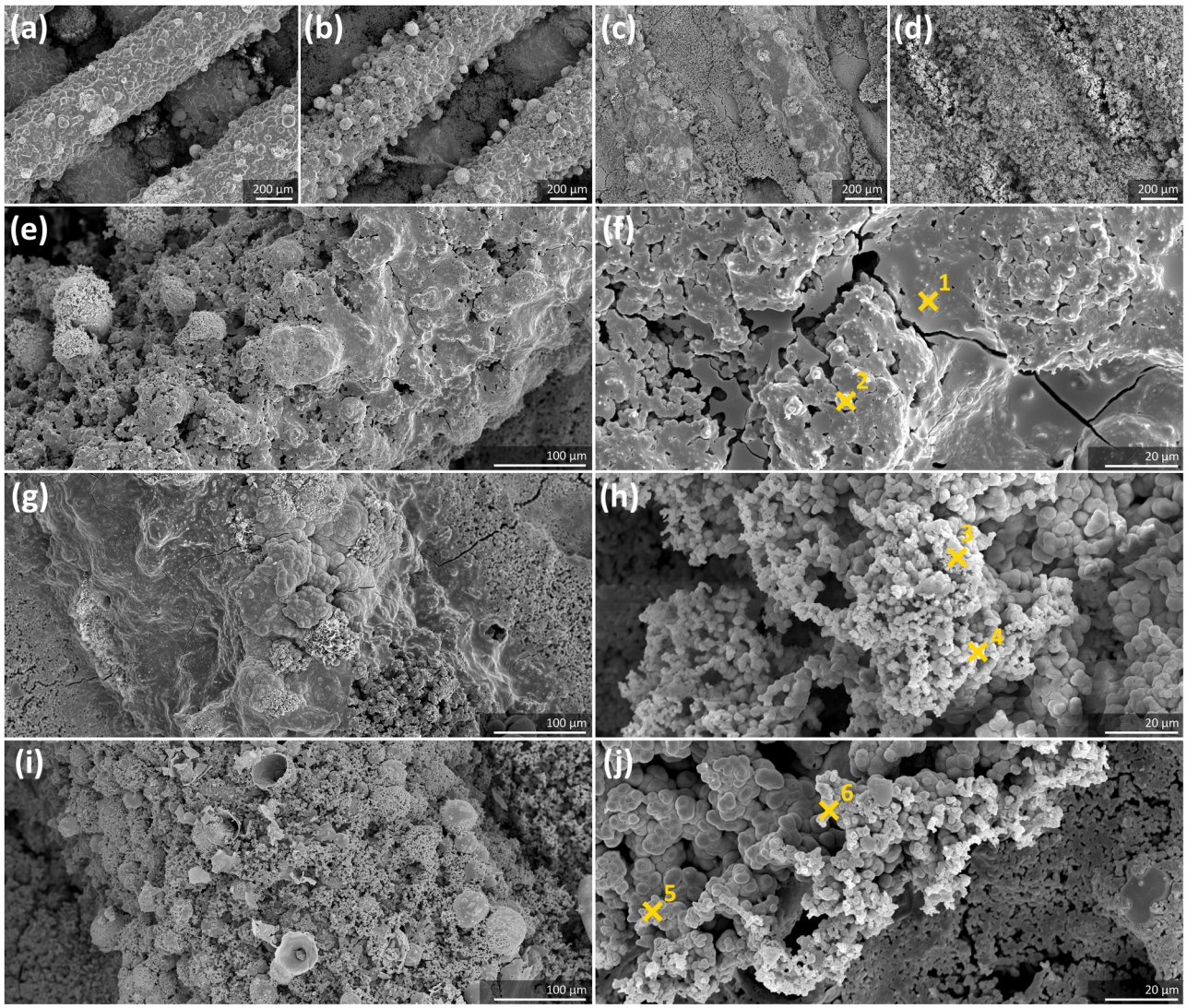

Fig. 6. The morphologies of biodegradation products found on the top surface of the Fe-CaO composite specimens on days (a) 4, (b) 7, (c) 14, and (d) 28. The morphologies of the biodegradation products on the struts at higher magnifications on days (e, f) 7, (g, h) 14, and (i, j) 28. Each number with a cross sign indicates the location of EDS spot analysis.

designed for the sustainable development of Fe-based bone-substituting biomaterials. The composite scaffolds, fabricated using DIW, were 70 % porous and contained the α-Fe and CaO phases. The composite scaffolds were biodegradable at a rate of 0.11 mm/year, while maintaining their mechanical properties (σ_y = 4–6 MPa and E = 0.1–0.3 GPa) within the range of human trabecular bone (σ_y = 0.1–30 MPa and E = 0.01–3 GPa [59]). The scaffolds demonstrated apatite-forming ability in r-SBF, as indicated by the formation of the HAp phase. The scaffolds exhibited cytocompatibility towards preosteoblasts and promoted osteogenic differentiation as well as *in vitro* mineralization. Additionally, the scaffolds demonstrated bactericidal activity against the MSSA and MDR-SA strains, and inhibited bacterial attachment, thereby delaying biofilm formation. The biofunctional properties of the porous Fe-CaO composite scaffolds underscore their potential as sustainable bioactive biomaterials for bone tissue regeneration and infection prevention.

4.1. *Sustainable AM of porous biodegradable Fe-eggshell bone substitutes*

AM has emerged as a sustainable option for the fabrication of medical devices. It offers the capability for the on-demand production of personalized biomaterials tailored to individual patients. With its additive characteristics, AM can precisely deposit materials at specific locations for intended biofunctionalities, minimizing scrap material. A notable AM technique is DIW, which has been utilized to create interconnected porous titanium (Ti) and Fe-based alloys for orthopedic applications [20,27,31,60]. The versatility of DIW in fabricating diverse materials and multi-material parts has been well recognized [61,62]. In this study, we used DIW for the fabrication of the porous Fe-based scaffolds containing eggshell particles for bone substitution. The use of recycled waste materials, such as eggshells, as raw sources for AM of biomaterials, was aimed to promote sustainable advances in bone tissue engineering.

Synthetic bioceramics, such as α-TCP [63], HAp [31,64], β-TCP [65,66], calcium silicate ($CaSiO_3$) [67], akermanite [32], and bredigite [29,30], have been used to enhance the bioactivity and biodegradation behavior of Fe-based bone substitutes. However, the synthesis of these bioceramics is lengthy and environmentally unsustainable. The processes include dissolving cation and anion components (*e.g.*, Ca^{2+} and PO_4^{3-}), slowly combining the aqueous solutions under alkaline conditions, followed by aging, suspension separation, washing, drying, and high-temperature sintering [68]. Alternative "green" synthesis methods, such as acid-free, hydrothermal processes utilizing non-hazardous substances, have also been explored [69]. The strategy adopted in this study, involving the use of recycled bioactive waste materials, such as

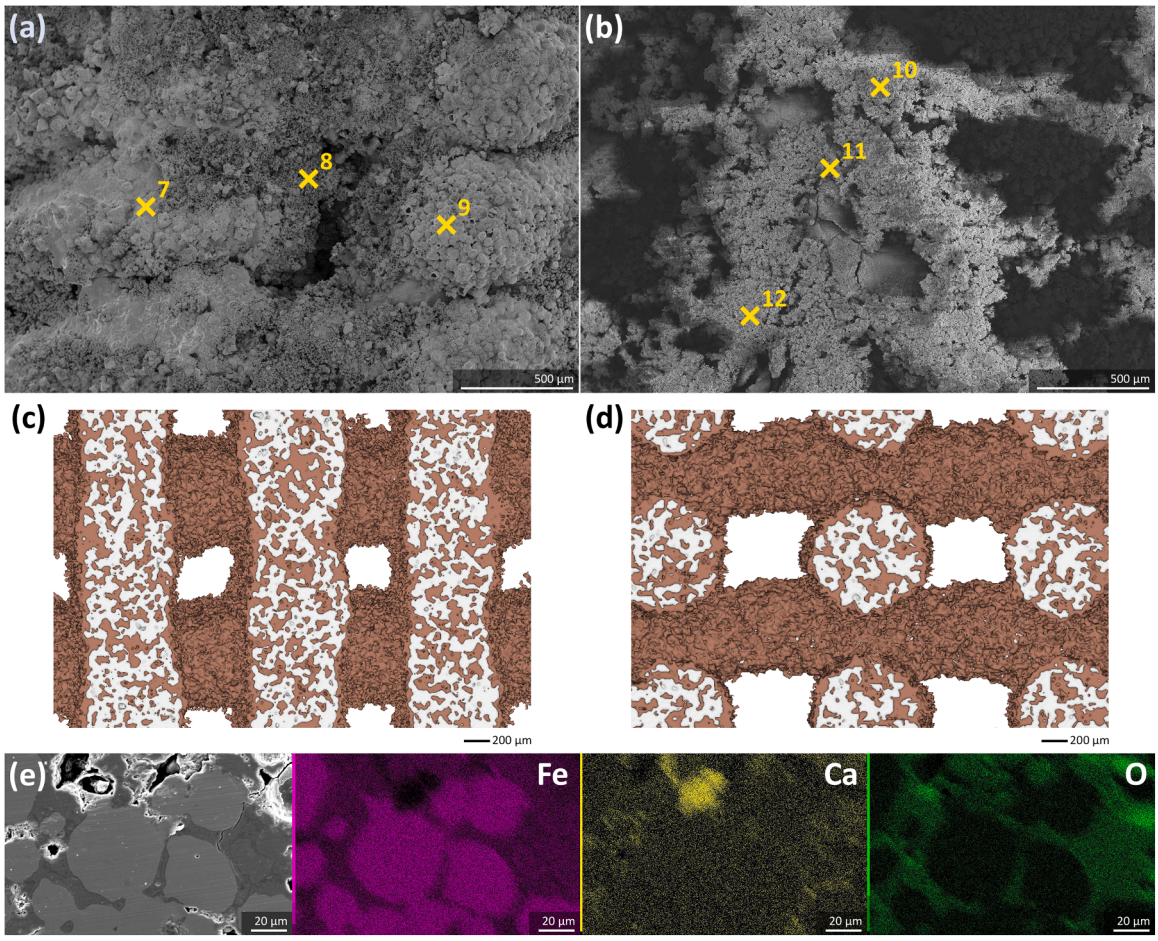

Fig. 7. The morphologies of the biodegradation products found on the lateral surface of the Fe-CaO composite specimens on days (a) 1 and (b) 28. The number with a cross sign indicates the location of EDS spot analysis. The cross-sections of the Fe-CaO composite specimens after 28 days of immersion as visualized by (c, d) µCT and (e) SEM with EDS mapping analysis.

Table 2
The chemical compositions of the biodegradation products of the porous Fe-CaO composite specimens (wt%), as determined by EDS spot analysis (shown in Figs. 6 and 7, with an accuracy of ±2%).

Fe-CaO	EDS point	C	O	P	Ca	Fe
Day 7 – top surface	**1**	15.73	3.51	-	0.62	80.14
	2	14.90	14.45	-	4.64	66.02
Day 14 – top surface	**3**	16.58	33.05	-	10.11	40.26
	4	11.94	26.93	-	17.26	43.87
Day 28 – top surface	**5**	23.78	14.70	-	21.20	40.32
	6	10.46	11.25	-	35.43	42.85
Day 1 – lateral surface	**7**	17.52	19.93	-	15.89	46.65
	8	10.07	34.38	-	47.86	7.68
	9	62.35	13.93	-	-	23.72
Day 28 – lateral surface	**10**	6.57	29.80	8.17	55.46	-
	11	1.01	6.63	18.13	74.23	-
	12	3.38	14.19	12.84	62.12	7.48

eggshells, presents a more sustainable alternative by eliminating the energy-intensive steps in the preparation of synthetic bioceramics. Moreover, the use of recycled bioactive waste materials for AM enables the *in situ* fabrication of porous biomaterials with specific geometrical structures for bone substitution, in line with circular economy principles and promoting waste valorization.

Eggshells are essentially $CaCO_3$ [40], which can be transformed into bone-substituting biomaterials. Eggshell particles have been used for maxillofacial bone repair *in vivo* [70]. They have been incorporated into hydrogels for *in vivo* bone tissue regeneration [43,44] and directly recycled into HAp and β-TCP powders [45,71,72]. More recently, eggshell particles have been utilized as the starting material for the DIW of porous HAp scaffolds [73]. Despite the promising biofunctionalities of eggshells and the derived HAp, they are inherently brittle [73], and thus require improvements for load-bearing applications.

We blended eggshells with Fe particles for DIW, harnessing the advantages of both materials in properties to create bioactive yet ductile Fe-eggshell scaffolds [20]. A successful DIW process requires the selection of an appropriate viscoelastic binder that enables the continuous extrusion of the feedstock with blended powder particles. The developed Fe-eggshell ink, containing a hypromellose binder (Fig. 1) that has been used in DIW for other materials [74–76] was shown to have a shear-thinning behavior (**Figure S2**). In addition to choosing the right binder, the volume ratio of the powder to the binder is another critical parameter to ensure a robust green-body structure (Fig. 2**a-c**). After DIW, the Fe-eggshell scaffolds underwent a post-AM heat treatment, involving (*i*) polymeric debinding at 350 °C, (*ii*) the phase transformation of eggshell $CaCO_3$ into CaO starting from 650 °C (**Figure S1**), and (*iii*) the fusion of powder particles at 1200 °C.

The sintered composite scaffolds exhibited a bimodal pore size distribution, characterized by the interconnected macro-pores in the strut spacing and micro-pores inside the struts (Fig. 2**d-f**). Such a pore size distribution is conducive to bone tissue regeneration [77]. Moreover, the scaffold architecture with the 0°/90° pattern provides a concave curvature at the intersections between the struts, which has been reported to attract the initiation of tissue growth *in vivo* in a sheep tibia

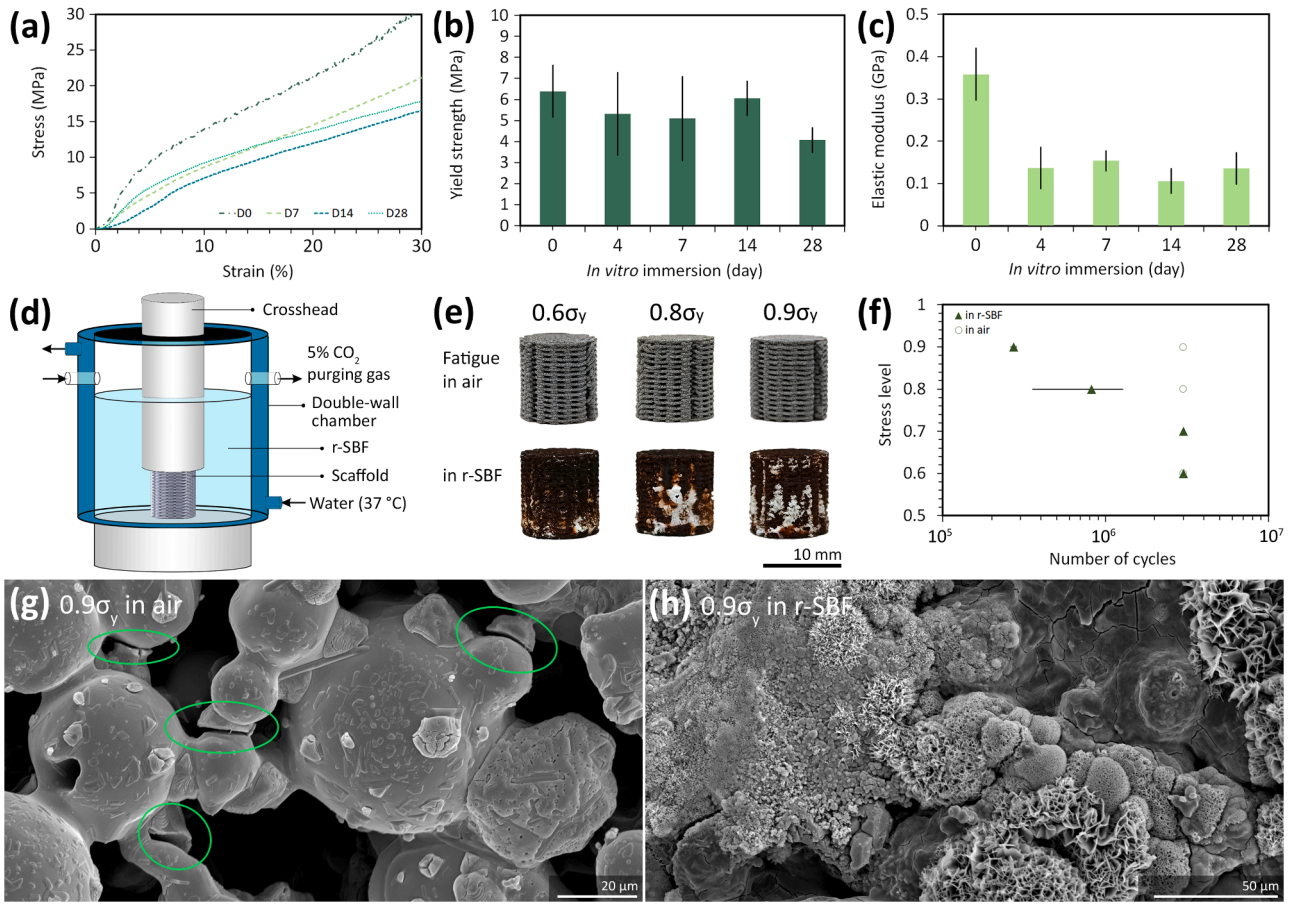

Fig. 8. The biodegradation-affected compressive mechanical properties of the porous Fe-CaO composite specimens: (a) Uniaxial stress-strain curves and time evolution of the (b) yield strength and (c) elastic modulus. The bars represent the mean and the error bars indicate the standard deviation. (d) A schematic illustration of the biodegradation fatigue test setup. (e) The visual inspection of the specimens after cyclic loading at different stress levels in air and in r-SBF. (f) the S-N curve. Morphologies of the powder particles after cyclic loading at $0.9\sigma_y$ (g) in air and (h) in r-SBF. The green ovals show the locations of cracks.

defect model [78]. Although macro-pore sizes in a range of 300–600 μm are recommended, a recent study on DIW Ti6Al4V scaffolds has reported that sub-300 μm pore sizes improve *in vitro* cell adhesion, proliferation, and differentiation [60]. Smaller pore sizes may benefit early-stage bioactivity, however, designating small macro-pore sizes to Fe-based scaffolds must be carefully deliberated, because reducing macro-pore sizes and overall porosity will slow down the biodegradation, which is not desirable for biodegradable iron-based materials.

Our composite scaffolds were primarily composed of α-Fe and CaO, with a minor presence of $Ca_2Fe_2O_5$ (Fig. 2**h**) at the interface between the two dominant phases. The scaffolds featured a uniform distribution of CaO particles throughout the α-Fe matrix (Fig. 2**i-j**). On the cross-section, Fe was seen to have diffused into CaO particles (Fig. 3**b**). The Ca-Fe-O ternary diagram confirms the possible formation of the $Ca_2Fe_2O_5$ phase at 900°C [79].

In this study, we selected the Fe powder with particle sizes of < 63 μm and eggshell powder with particle sizes of < 45 μm for DIW. Gradation of particle sizes, such as a combination of fine and coarse particles, will increase packing density, green density and sintered density [80,81], which may improve mechanical properties and modulate biodegradation behavior. Additionally, surface features governed by retained particle morphology and sizes may influence cell attachment and bioactivity [82]. In addition to particle size distribution, the macro-pore size distribution of scaffolds may be improved by exploring a functionally graded hierarchical porous structure design [25] that combines larger outer pores for vascularization and smaller internal pores (*e.g.*, sub-300 μm [60]) for optimum biodegradation, mechanical properties and bioactivity.

4.2. Biodegradation behavior

The Fe-CaO composite scaffolds exhibited a biodegradation rate of 0.11 mm/y after 28 days of immersion in r-SBF. The biodegradation rate of the porous Fe-CaO composite scaffolds requires an elevation to reach the expected biodegradation rate of an ideal bone substitute (*i.e.*, 0.2–0.5 mm/year [83]). This can be achieved by adding Mn that has a lower standard electrode potential to create an FeMn-based composite with a higher biodegradation rate [21,64]. Nevertheless, the biodegradation rate is comparable to the values of the porous Fe-15 vol% akermanite composite [32], porous Fe- 30 wt% $CaSiO_3$ composite [67,84], and solid Fe-5 wt% bredigite composite [29]. The value is 3 to 4 times higher than that of solid Fe-5 wt% HAp/TCP composite [66] and 2 times higher than that of geometrically similar porous Fe [20] (Table 3).

The accelerated biodegradation of the porous Fe-CaO composite was due to the combined effects of porosity and the dispersion of the CaO phase in the α-Fe matrix. The interconnected macro-pore spacing of the scaffolds and the micro-pores in the struts provide a larger available surface area for biodegradation. Once exposed to a physiological solution, the CaO phase reacts directly with water and transforms into calcium hydroxide ($Ca(OH)_2$, Eq. 4), which has a higher solubility (*i.e.*, $K_{sp} = 5 \times 10^{-6}$ [85]) than CaP-based bioceramics (*i.e.*, $K_{sp} = 2 \times 10^{-33}$ [85]):

$$CaO_{(s)} + H_2O_{(l)} \rightarrow Ca(OH)_{2\ (s)} \quad (4)$$

The biodegradation of the porous Fe-CaO composite started at a high rate in the first 4 d of immersion (*i.e.*, 6 % mass loss, Fig. 4**b**). The

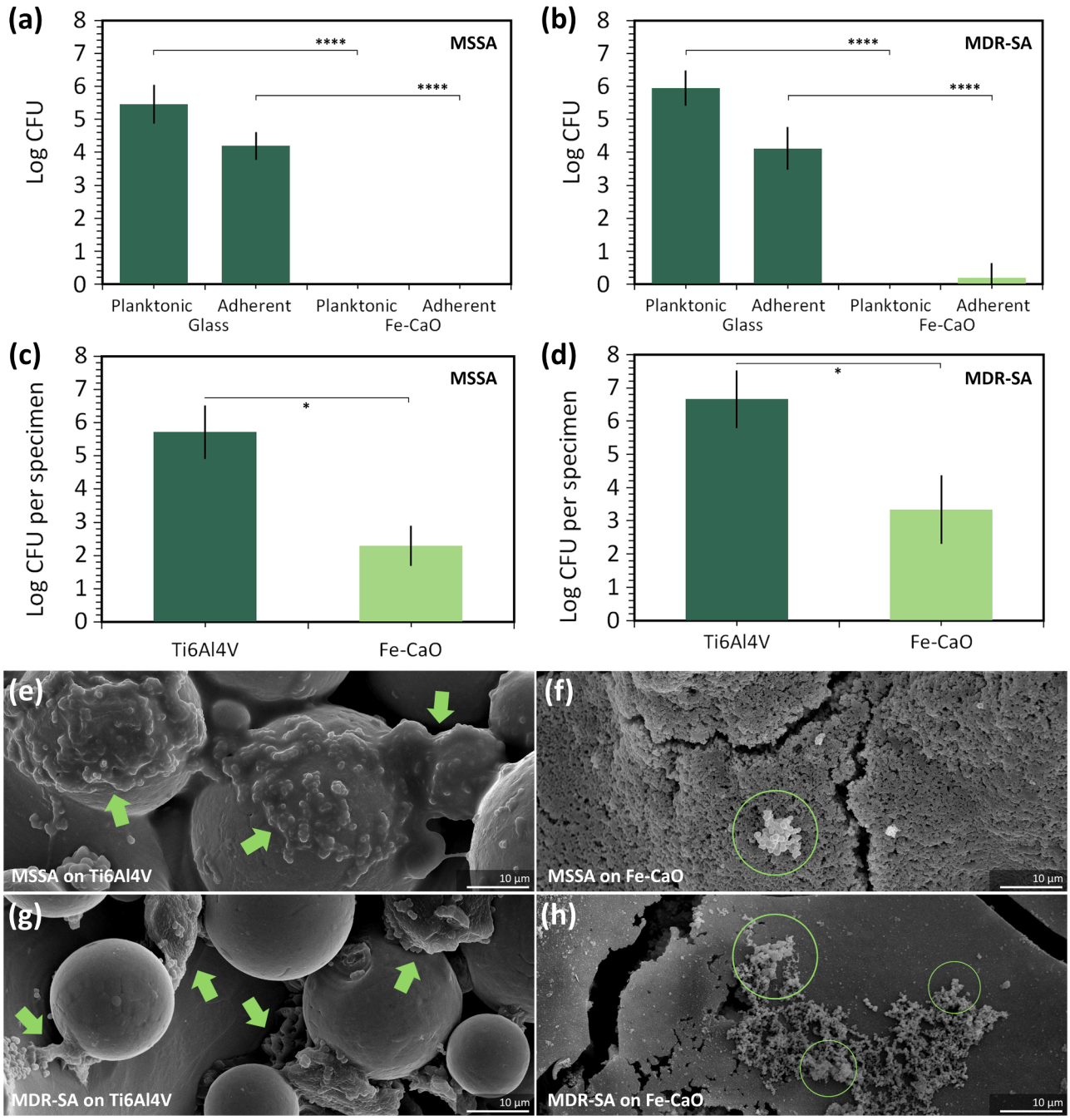

Fig. 9. The antibacterial properties of the Fe-CaO composite specimens. Bactericidal activity against (a) MSSA and (b) MDR-SA strains after 4 h culture (**** = $p < 0.0001$). The specimens were inoculated with 8.5×10^4 CFU per specimen. The numbers of adherent (c) MSSA and (d) MDR-SA bacteria after 4 h culture in the CDC biofilm reactor (* = $p < 0.05$). After 4 h, the concentration of planktonic bacteria in the biofilm reactor was 1.3×10^7 CFU (MSSA) and 1×10^7 CFU (MDR-SA). The bars represent the mean and the error bars indicate the standard deviation. The morphologies of adherent MSSA on the (e) Ti6Al4V alloy and (f) Fe-CaO composite specimens. The morphologies of adherent MDR-SA on the (g) Ti6Al4V alloy and (h) Fe-CaO composite specimens.

concentrations of Fe^{2+} and Ca^{2+} reached their peaks at day 4 (Fig. 4**c-d**). After that, biodegradation slowed down, as evidenced by the trend of the mass loss (Fig. 4**b**). The decreases in the concentrations of the soluble Fe^{2+} and Ca^{2+} ions over time indicated that these ions participated in the formation of the biodegradation products.

After 1 d of immersion (Fig. 4**a**), the biodegradation products covered the surface of the struts. The density of these products increased with immersion time, as is clear from the SEM images (Fig. 6), thereby preventing direct oxidation of the composite surface. This was consistent with the changes observed in the electrochemical responses of the composite specimens. The increasing OCP values (Fig. 4**g**), R_p value (Fig. 4**h**), and impedance modulus values in the low frequency region (*i.e.*, 0.01 Hz) with time (Fig. 4**i-j**) are indicative of increasing charge transfer resistance at the metal-to-electrolyte/biodegradation product interface related to increasing biodegradation product formation with time [86]. This is corroborated by the impedance modulus value increase in the mid-frequency region (*i.e.*, 10 Hz, Fig. 4**i-j**) indicative of the evolution of capacitive and resistive behavior during the apparent formation of biodegradation products, *i.e.*, growth and partial dissolution with time [87]. The Nyquist plots (Fig. 4**k**) infer that active biodegradation occurred under mixed kinetic-diffusion control, with a quarter-circle arc showing an increasing diameter with exposure time,

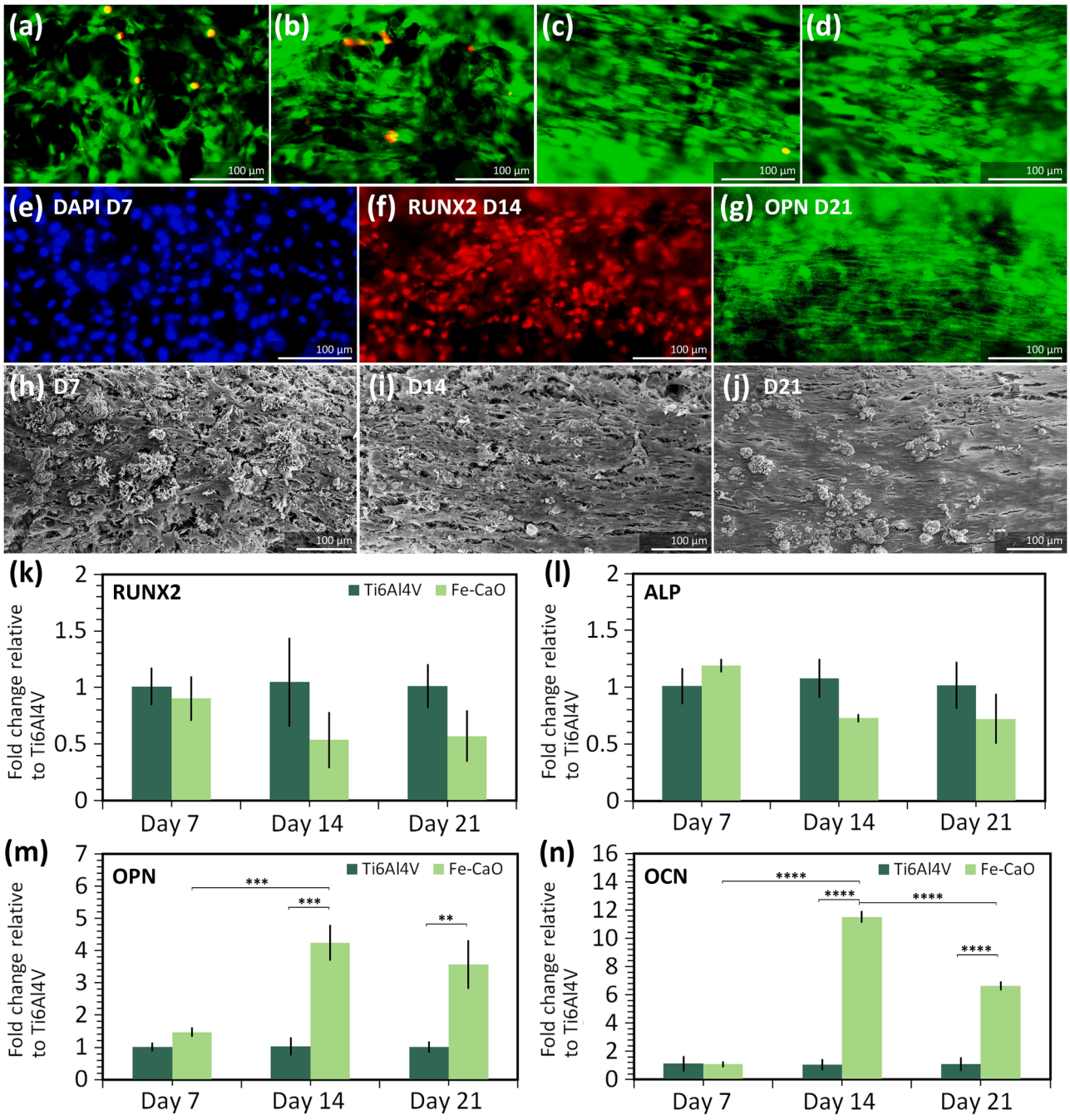

Fig. 10. The cytocompatibility and osteogenic potential of the Fe-CaO composite specimens: Live-dead staining on days (a) 1, (b) 4, (c) 7, and (d) 14. (Immuno) staining of (e) DAPI on day 7, (f) RUNX2 on day 14, and (g) OPN on day 21. The morphologies of the cells on the struts of the composite specimens, as visualized by SEM on days (h) 7, (i) 14, and (j) 21. The (k) RUNX2, (l) ALP, (m) OPN, and (n) OCN expression of the cells on the composite specimens, in a fold change, relative to the Ti6Al4V alloy specimens. The bars represent the mean and the error bars indicate the standard deviation (** = $p < 0.01$, *** = $p < 0.001$, **** = $p < 0.0001$).

indicative of increasing polarization resistance [88]. This is in line with the impedance modulus value at low- and mid-frequencies (Fig. 4**i-j**) related to an increasing charge transfer resistance with increasing biodegradation product formation with time. In the lower frequency region, the Nyquist plots exhibited straight lines with a Warburg impedance angle close to 45° (Fig. 4**k**). This indicates that the biodegradation mechanism is governed by mixed kinetic and charge transfer control related to diffusion processes through the relatively dispersed and porous biodegradation products [52].

The formation of γ-FeOOH products is expected from the biodegradation of porous Fe-based biomaterials [89]. This phase is known for passivating the material surface and slowing down the corrosion of Fe [24]. In addition to γ-FeOOH, Ca-based products were observed (Fig. 5). The $CaCO_3$ phase was present at all time points, similar to the observations reported for the biodegradation of porous Fe-akermanite [32]. The formation of the $CaCO_3$ phase can be related to the high concentration of Ca^{2+} and the availability of monohydrogen carbonate (HCO_3^-) and carbonate (CO_3^{2-}) ions in the test medium (Eqs. 5-6) [90]:

$$Ca^{2+}_{(aq)} + CO^{2-}_{3(aq)} \rightarrow CaCO_{3\,(s)} \quad (5)$$

or

$$Ca^{2+}_{(aq)} + 2HCO^{-}_{3(aq)} \rightarrow CaCO_{3\,(s)} + CO_{2\,(g)} + H_2O_{(l)} \quad (6)$$

Table 3
Biodegradation rate, mechanical properties, and cytocompatibility of the DIW porous Fe-CaO composite scaffolds in comparison with those of DIW Fe and Fe-bioceramic composites found in the literature.

Materials	Porosity or pore size	Biodegradation rate	Compressive yield strength	Compressive elastic modulus	Cytocompatibility
DIW Fe-20 vol% eggshell	70% (410 μm)	0.107 ± 0.003 mm/y or 15 ± 1% mass loss at day 28	6 ± 1 MPa at day 0 4.1 ± 0.6 MPa at day 28	0.36 ± 0.06 GPa at day 0 0.14 ± 0.04 GPa at day 28	Cytocompatible and osteogenic
DIW Fe [20]	67% (410 μm)	0.05 ± 0.01 mm/y at day 28	7.2 ± 0.4 MPa at day 0 9.4 ± 0.9 MPa at day 28	0.6 ± 0.1 GPa at day 0 0.7 ± 0.2 GPa at day 28	Cytotoxic
DIW Fe [27]	50 μm	0.005 ± 0.002 mm/y at day 14	15.1 ± 0.8 MPa at day 0 10.0 ± 0.2 MPa at day 14	0.63 ± 0.05 GPa at day 0 0.34 ± 0.02 GPa at day 14	N/A
	300 μm	0.042 ± 0.001 mm/y at day 14	9.5 ± 0.9 MPa at day 0 5.2 ± 0.5 MPa at day 14	0.33 ± 0.02 GPa at day 0 0.21 ± 0.01 GPa at day 14	N/A
DIW Fe-5 wt% HAp [31]	70%	3.2 ± 0.2% mass loss at day 21	25 ± 4 MPa at day 0 11 ± 3 MPa at day 21 *Compressive strength	N/A	N/A
DIW Fe-7.5 wt% HAp [31]	70%	3.3 ± 0.3% mass loss at day 21	7.5 ± 0.3 MPa at day 0 19 ± 2 MPa at day 21 *Compressive strength	N/A	N/A
DIW Fe-15 vol% akermanite [32]	69% (410 μm)	0.11 ± 0.02 mm/y at day 28	3.4 ± 0.5 MPa at day 0 1.5 ± 0.3 MPa at day 14	0.23 ± 0.05 GPa at day 0 0.17 ± 0.07 GPa at day 28	Cytocompatible and osteogenic
DIW Fe-20 vol% akermanite [32]	71% (410 μm)	0.13 ± 0.01 mm/y at day 28	2.9 ± 0.9 MPa at day 0 0.8 ± 0.2 MPa at day 14	0.17 ± 0.05 GPa at day 0 0.13 ± 0.05 GPa at day 28	Cytocompatible and osteogenic
SLM Fe-5 wt% Bredigite [29]	Bulk	0.16 ± 0.02 mm/y at day 28	200 ± 11 MPa at day 0	N/A	Cytocompatible
SLM Fe-7.5 wt% Bredigite [29]	Bulk	0.31 ± 0.02 mm/y at day 28	161 ± 14 MPa at day 0	N/A	Cytocompatible

In addition to $CaCO_3$, carbonatious HAp formed on the top surface of the specimens after 28 days (Fig. 5**a**) while pure HAp was detected on the lateral surface of the specimens at all time points (Fig. 5**b**). The *in situ* apatite-forming ability of the porous Fe-CaO composite scaffolds during *in vitro* biodegradation underscores their potential for bone substitution. This advantage was not observed in other Fe-based composite scaffolds containing synthetic bioceramics [21,29,30,32].

Furthermore, the $Ca_2Fe_2O_5$ phase, minorly formed in the composite scaffolds, is not particularly stable in physiological condition and is expected to decomposed into Ca^{2+} and Fe^{3+} ions (Eq. 7) [79].

$$Ca_2Fe_2O_{5(s)} + 5H_2O_{(l)} \rightarrow 2Ca^{2+}_{(aq)} + 2Fe^{3+}_{(aq)} + 10OH^-_{(aq)} \quad (7)$$

It has been reported that SBF with ion concentrations identical to those of human blood plasma (*i.e.*, pH ≥ 7.65) exhibits a degree of supersaturation conducive to apatite formation [91]. Moreover, the ability of biomaterials to form apatite can be enhanced through the release of Ca^{2+} [92]. Although the global pH in r-SBF remained relatively stable, the local pH values were elevated in the initial hours of immersion (Fig. 4**f**), as a result of the rapid dissolution of the CaO phase (Eq. 8). In addition to the alkaline local environment, the concentration values of Ca^{2+} in r-SBF at all time points exceeded the value in the original medium (Fig. 4**d**). These observations indicate that all the conditions necessary for HAp formation (Eq. 9) were met during the biodegradation of the porous Fe-CaO composite:

$$CaO_{(s)} + H_2O_{(l)} \rightarrow Ca(OH)_{2\ (s)} \rightarrow Ca^{2+}_{(aq)} + 2OH^-_{(aq)} \quad (8)$$

$$5Ca^{2+}_{(aq)} + 3PO^{3-}_{4\ (aq)} + OH^-_{(aq)} \rightarrow Ca_5(PO_4)_3OH_{(s)} \quad (9)$$

$CaCO_3$ as a biodegradation product can be a precursor of apatite formation as well. In the absence of Mg and Si, the $CaCO_3$ phase tends to be less stable [93–95], and may undergo carbonate–phosphate exchange [96], resulting in the formation of the carbonatious HAp phase (Eq. 10), as observed on the top surface of the Fe-CaO specimens after 28 days of immersion:

$$CaCO_{3\ (s)} + 3HPO^{2-}_{4\ (aq)} + H_2O_{(aq)} \leftrightarrow Ca_5(PO_4)_{(3-x)}OH_{(s)} + (5-x)CO^{2-}_{3\ (aq)} \quad (10)$$

Altogether, the biodegradation behavior and apatite-forming ability of the porous Fe-CaO composite scaffolds highlight their potential as bone-substituting biomaterials.

4.3. Mechanical performance

Bone-substituting biomaterials are expected to maintain their structural integrity as they degrade, particularly at the initial stages of the bone healing process. The compressive mechanical properties of the Fe-CaO composite scaffolds (σ_y = 4–6 MPa and E = 0.1–0.3 GPa) were within the range of the trabecular bone (*i.e.*, σ_y = 0.1–30 MPa and E = 0.01–3 GPa [59]) even after 28 days of *in vitro* immersion (Fig. 8). The initial yield strength and elastic modulus of the porous Fe-CaO composite (with 9 vol% CaO) were higher than those of geometrically similar porous Fe-akermanite composite specimens (with 5–20 vol% akermanite) [32]. Their good mechanical properties are attributed to the greater diffusion depth of Fe into the CaO phase (*i.e.*, nearly 10 μm) than that of Fe into the akermanite phase (*i.e.*, 2 μm [32]). As expected, biodegradation reduced the mechanical properties of the specimens. The decreasing trend of the yield strength and elastic modulus of the Fe-CaO specimens observed was similar to that of other porous Fe-based composites [21,32,65].

The biodegradation fatigue strength of the Fe-CaO scaffolds (= $0.7\sigma_y$) is higher than those of porous Fe (= $0.65\sigma_y$ [97]), porous Fe35Mn alloy (= $0.6\sigma_y$ [98]), and porous WE43 Mg alloy (= $0.2\sigma_y$ [99]). The fatigue strength of the composite at 1 million cycles (*i.e.*, (= $0.7–0.8\sigma_y$) is better than that of porous Ti6Al4V scaffolds (= $0.6\sigma_y$ [100]). The fatigue strength of the porous Fe-CaO composite scaffolds is comparable to those of bone screw implants that are often evaluated up to 1 million cycles [101,102].

The fatigue strength of the porous Fe-CaO composite scaffolds at 3 million cycles decreased from $0.9\sigma_y$ in air to $0.7\sigma_y$ in r-SBF. Biodegradation reduces the fatigue strength of the composite, which is completely different when compared to porous Zn (with a fatigue strength of $0.7\sigma_y$ in air and improved to $0.8\sigma_y$ in r-SBF [103]). Although HAp precipitated during the biodegradation of the Fe-CaO composite, it did not aid in enhancing the mechanical properties. This is likely because the HAp phase was mainly present on the periphery of the specimens and in the form of loose powder particles (Figs. 6**j** and 7**b**). A strategy to consolidate the apatite formed during the biodegradation of such materials should be explored to enhance the mechanical properties of the composite.

4.4. Antibacterial properties

The porous Fe-CaO composite scaffolds developed in this study exhibited promising biofunctionalities relevant to infection prevention. The scaffolds (*i*) displayed bactericidal activity against both MSSA and MDR-SA strains, achieving at least 5.5-log and 3.9-log reductions in the number of CFU of planktonic and adherent bacteria, respectively (Fig. 9**a-b**), and (*ii*) prevented bacterial adhesion (Fig. 9**c-d**), thereby delaying biofilm formation (Fig. 9**e-h**). The *in vitro* antibacterial performance of the porous Fe-CaO composite scaffolds was comparable to that of antibacterial surfaces containing Ag/Zn and Ag/Fe nanoparticles on Ti6Al4V alloy tested against MRSA [104,105]. Importantly, the pure Fe scaffolds did not demonstrate any antibacterial activity against the MSSA and MDR-SA strains (**Figure S3**). Similar observations have been reported in other studies, where pure Fe and FeMn alloy scaffolds exhibited no antibacterial activity against several laboratory bacterial strains of *S. aureus* and *Escherichia coli* [106–108].

The antibacterial properties of the porous Fe-CaO composite scaffolds were clearly due to the presence of the CaO phase. The antibacterial properties of CaO micro- and nanoparticles have been reported in the literature [109–111]. The antibacterial mechanism involved oxidative stresses on bacterial cells and the alkaline environment, resulting from CaO particle hydration and the release of Ca^{2+} ions [110,111]. At the microscale, the pH level surrounding the CaO particles is higher, which can damage the bacteria cell membrane [111]. Bacterial membrane damage was confirmed following exposure to extracts of the Fe-CaO composite specimens (**Figure S4**). Based on our observations, including the local pH measurement (Fig. 4**c**), the Ca^{2+} ions release profile in r-SBF (Fig. 4**d**) and the availability of the CaO phase in the composite even after 28 days biodegradation (Fig. 7**e**), the porous Fe-CaO composite scaffolds have the potential for relatively long-term infection prevention.

Implant-associated infections have become increasingly challenging to treat due to the rise of antibiotic-resistant bacteria. Biomaterials endowed with bactericidal properties against antimicrobial resistant bacterial strains have been developed [104,105]. However, these challenges persist. Studies that reported bactericidal effects *in vitro* may not translate to similar outcomes *in vivo* [112]. The concentration of antibacterial agents on implants must be tuned to ensure cytocompatibility while clearing all signs of infections. The antibacterial agents should not elicit hyperimmune responses that can counteract the necessary immune response needed to fight the infection [112]. Moreover, selection of suitable *in vivo* infection models is crucial for the translation of such biomaterials. Although the initial bactericidal action of the porous Fe-CaO composite is crucial for preventing post-surgical infection, its effect in terms of modulating the immune response still requires a thorough investigation. The immune system's reaction to implants post-surgery is beneficial not only for eliminating residual infection threats but also for facilitating the bone healing process [113].

4.5. Cytocompatibility and osteogenic potential

The porous Fe-CaO composite scaffolds developed were compatible with the preosteoblasts MC3T3-E1 cells, allowing for cell adhesion, proliferation, and differentiation (Fig. 10**a-g**). The cytocompatibility of the porous Fe-CaO composite specimens for preosteoblasts was notably improved as compared to the cytotoxic pure Fe scaffolds (**Figure S5**). This improvement could be attributed to the sustained release of Ca^{2+} ions from the eggshell-derived CaO phase, mitigating the cytotoxic effects associated with Fe^{2+} ion release. Ca is a vital element for the development of healthy bone tissue. Osteoblast growth and differentiation are influenced by the Ca signaling pathway [114]. Several studies have reported the osteogenic properties of various Ca–doped biomaterials [115,116]. Porous Fe-CaO composite scaffolds, developed in this study, offer a platform that continuously releases Ca^{2+} ions (Fig. 4**b**), potentially benefiting patients with bone defects and Ca deficit.

Ample availability of Ca^{2+} ions is also a key to successful apatite mineralization, provided that the right Ca/P balance is also ensured [117]. Although the Fe-CaO composite scaffolds exhibited similar levels of the early osteogenic markers RUNX2 and ALP (Fig. 10**k-l**) as compared to porous Ti6Al4V, the composite specimens significantly upregulated the expression of the late osteogenic markers OPN and OCN (Fig. 10**m-n**). OPN and OCN are involved in the onset of the mineralization phase, which is associated with mature osteoblasts [118,119], confirming the osteogenic capacity of the composite scaffolds. Taken together, our results demonstrated the biofunctionalities of the sustainable DIW porous Fe composite as a bone-substituting biomaterial containing eggshell-derived CaO.

5. Conclusions

We developed porous Fe composite scaffolds incorporating 20 vol% of waste-derived eggshell particles for bone substitution. The Fe-eggshell scaffolds were fabricated using the DIW technique. The composite scaffolds were mainly composed of the α-Fe and CaO phases. The latter phase was derived *in situ* from eggshell $CaCO_3$. The scaffolds had an absolute porosity of 70 % and a biodegradation rate of 0.11 mm/y. They were able to maintain their mechanical properties in the range of the trabecular bone as they biodegraded. The porous Fe-CaO composite scaffolds exhibited antibacterial activities against MSSA and MDR-SA strains, promising to be effective in the prevention of implant-associated infections. Furthermore, the scaffolds demonstrated their apatite-forming ability during *in vitro* immersion tests in r-SBF, which is conducive to bone tissue regeneration. As compared to the gold-standard permanent bone implant material (Ti6Al4V), the composite specimens developed here facilitated the adhesion, proliferation, and differentiation of preosteoblasts MC3T3-E1, while also upregulating the expression of late osteogenic markers related to mineralization.

CRediT authorship contribution statement

Niko E. Putra: Writing – review & editing, Writing – original draft, Methodology, Investigation, Formal analysis, Conceptualization. **Raphaëlle Youf:** Writing – review & editing, Validation, Methodology, Investigation, Formal analysis, Data curation. **Vahid Moosabeiki:** Writing – review & editing, Software, Methodology, Investigation. **Marius A. Leeflang:** Software, Methodology, Investigation. **Maria Klimopoulou:** Methodology, Investigation. **Mohammad J. Mirzaali:** Writing – review & editing, Supervision, Resources. **Arjan Mol:** Writing – review & editing, Resources. **Martijn Riool:** Writing – review & editing, Validation, Supervision, Resources, Methodology. **Lidy E. Fratila-Apachitei:** Writing – review & editing, Supervision, Resources, Methodology. **Jie Zhou:** Writing – review & editing, Supervision, Resources, Methodology. **Iulian Apachitei:** Supervision, Resources, Project administration. **Amir A. Zadpoor:** Writing – review & editing, Supervision, Resources, Funding acquisition.

Declaration of competing interest

The authors declare that they have no known competing financial interests or personal relationships that could have appeared to influence the work reported in this paper.

Amir A Zadpoor is an Editorial Board Member for this journal and was not involved in the editorial review or the decision to publish this article.

Acknowledgments

This work is part of the DARTBAC project number with project number NWA.1292.19.354 of the research program NWA-ORC, which is (partly) financed by the Dutch Research Council (NWO). The authors

thank Mr. Roy Awater at Materials Physics Lab, Department of Aerospace Structures and Materials, Delft University of Technology for his assistance in the TGA measurement. Mr. Ruud Hendrikx at the Department of Materials Science and Engineering, Delft University of Technology is acknowledged for XRD analysis. Mr. Michel van den Brink at the Department of Process and Energy, Delft University of Technology is acknowledged for the ICP-OES analysis. The authors thank Mrs. Agnieszka Kooijman at the Department of Materials Science and Engineering, Delft University of Technology for her assistance in electrochemical measurements.

Supplementary materials

Supplementary material associated with this article can be found, in the online version, at doi:10.1016/j.actbio.2025.06.051.

References

[1] N.E. Putra, J. Zhou, A.A. Zadpoor, Sustainable sources of raw materials for additive manufacturing of bone-substituting biomaterials, Adv. Healthc. Mater. 13 (2024) 2301837, https://doi.org/10.1002/adhm.202301837.
[2] T. Peng, K. Kellens, R. Tang, C. Chen, G. Chen, Sustainability of additive manufacturing: an overview on its energy demand and environmental impact, Addit. Manuf. 21 (2018) 694–704, https://doi.org/10.1016/j.addma.2018.04.022.
[3] S. Ford, M. Despeisse, Additive manufacturing and sustainability: an exploratory study of the advantages and challenges, J. Clean. Prod. 137 (2016) 1573–1587, https://doi.org/10.1016/j.jclepro.2016.04.150.
[4] H.A. Colorado, E.I.G. Velásquez, S.N. Monteiro, Sustainability of additive manufacturing: the circular economy of materials and environmental perspectives, J. Mater. Res. Technol. 9 (2020) 8221–8234, https://doi.org/10.1016/j.jmrt.2020.04.062.
[5] L. Agnusdei, A. Del Prete, Additive manufacturing for sustainability: a systematic literature review, Sustain. Fut. 4 (2022) 100098, https://doi.org/10.1016/j.sftr.2022.100098.
[6] B. Peng, Y. Wei, Y. Qin, J. Dai, Y. Li, A. Liu, Y. Tian, L. Han, Y. Zheng, P. Wen, Machine learning-enabled constrained multi-objective design of architected materials, Nat. Commun. 14 (2023) 6630, https://doi.org/10.1038/s41467-023-42415-y.
[7] H. Pahlavani, K. Tsifoutis-Kazolis, M.C. Saldivar, P. Mody, J. Zhou, M.J. Mirzaali, A.A. Zadpoor, Deep learning for size-agnostic inverse design of random-network 3D printed mechanical metamaterials, Adv. Mater. 36 (2024) 1–18, https://doi.org/10.1002/adma.202303481.
[8] A.A. Zadpoor, J. Malda, Additive manufacturing of biomaterials, tissues, and organs, Ann. Biomed. Eng. 45 (2017) 1–11, https://doi.org/10.1007/s10439-016-1719-y.
[9] C. Culmone, G. Smit, P. Breedveld, Additive manufacturing of medical instruments: a state-of-the-art review, Addit. Manuf. 27 (2019) 461–473, https://doi.org/10.1016/j.addma.2019.03.015.
[10] N.E. Putra, M.J. Mirzaali, I. Apachitei, J. Zhou, A.A. Zadpoor, Multi-material additive manufacturing technologies for Ti-, Mg-, and Fe-based biomaterials for bone substitution, Acta Biomater. 109 (2020) 1–20, https://doi.org/10.1016/j.actbio.2020.03.037.
[11] M.J. Mirzaali, V. Moosabeiki, S.M. Rajaai, J. Zhou, A.A. Zadpoor, Additive manufacturing of biomaterials - design principles and their implementation, Materials (Basel) 15 (2022) 5457, https://doi.org/10.3390/ma15155457.
[12] M.H. Mobarak, M.A. Islam, N. Hossain, M.Z. Al Mahmud, M.T. Rayhan, N. J. Nishi, M.A. Chowdhury, Recent advances of additive manufacturing in implant fabrication – a review, Appl. Surf. Sci. Adv. 18 (2023) 100462, https://doi.org/10.1016/j.apsadv.2023.100462.
[13] L. Zhang, G. Yang, B.N. Johnson, X. Jia, Three-dimensional (3D) printed scaffold and material selection for bone repair, Acta Biomater. 84 (2019) 16–33, https://doi.org/10.1016/j.actbio.2018.11.039.
[14] G.L. Koons, M. Diba, A.G. Mikos, Materials design for bone-tissue engineering, Nat. Rev. Mater. 5 (2020) 584–603, https://doi.org/10.1038/s41578-020-0204-2.
[15] A.A. Zadpoor, Additively manufactured porous metallic biomaterials, J. Mater. Chem. B. 7 (2019) 4088–4117, https://doi.org/10.1039/c9tb00420c.
[16] Y. Li, J. Zhou, P. Pavanram, M.A. Leeflang, L.I. Fockaert, B. Pouran, N. Tümer, K. U. Schröder, J.M.C. Mol, H. Weinans, H. Jahr, A.A. Zadpoor, Additively manufactured biodegradable porous magnesium, Acta Biomater. 67 (2018) 378–392, https://doi.org/10.1016/j.actbio.2017.12.008.
[17] Y. Li, H. Jahr, K. Lietaert, P. Pavanram, A. Yilmaz, L.I. Fockaert, M.A. Leeflang, B. Pouran, Y. Gonzalez-Garcia, H. Weinans, J.M.C. Mol, J. Zhou, A.A. Zadpoor, Additively manufactured biodegradable porous iron, Acta Biomater. 77 (2018) 380–393, https://doi.org/10.1016/j.actbio.2018.07.011.
[18] Y. Li, P. Pavanram, J. Zhou, K. Lietaert, P. Taheri, W. Li, H. San, M.A. Leeflang, J. M.C. Mol, H. Jahr, A.A. Zadpoor, Additively manufactured biodegradable porous zinc, Acta Biomater. 101 (2020) 609–623, https://doi.org/10.1016/j.actbio.2019.10.034.
[19] J. Dong, P. Lin, N.E. Putra, N. Tümer, M.A. Leeflang, Z. Huan, L.E. Fratila-Apachitei, J. Chang, A.A. Zadpoor, J. Zhou, Extrusion-based additive manufacturing of Mg-Zn/bioceramic composite scaffolds, Acta Biomater. 151 (2022) 628–646, https://doi.org/10.1016/j.actbio.2022.08.002.
[20] N.E. Putra, M.A. Leeflang, M. Minneboo, P. Taheri, L.E. Fratila-Apachitei, J.M. C. Mol, J. Zhou, A.A. Zadpoor, Extrusion-based 3D printed biodegradable porous iron, Acta Biomater. 121 (2021) 741–756, https://doi.org/10.1016/j.actbio.2020.11.022.
[21] N.E. Putra, M.A. Leeflang, M. Klimopoulou, J. Dong, P. Taheri, Z. Huan, L. E. Fratila-Apachitei, J.M.C. Mol, J. Chang, J. Zhou, A.A. Zadpoor, Extrusion-based 3D printing of biodegradable, osteogenic, paramagnetic, and porous FeMn-akermanite bone substitutes, Acta Biomater. 162 (2023) 182–198, https://doi.org/10.1016/j.actbio.2023.03.033.
[22] D. Carluccio, C. Xu, J. Venezuela, Y. Cao, D. Kent, M. Bermingham, A.G. Demir, B. Previtali, Q. Ye, M. Dargusch, Additively manufactured iron-manganese for biodegradable porous load-bearing bone scaffold applications, Acta Biomater. 103 (2020) 346–360, https://doi.org/10.1016/j.actbio.2019.12.018.
[23] Y. Nie, G. Chen, H. Peng, S. Tang, Z. Zhou, F. Pei, B. Shen, In vitro and 48 weeks in vivo performances of 3D printed porous Fe-30Mn biodegradable scaffolds, Acta Biomater. 121 (2021) 724–740, https://doi.org/10.1016/j.actbio.2020.12.028.
[24] A. Al Sakkaf, F.S. Januddi, A.H.M. Yusop, H. Nur, Challenges in the use of Fe-based materials for bone scaffolds applications: perspective from in vivo biocorrosion, Mater. Today Commun. 33 (2022) 104564, https://doi.org/10.1016/j.mtcomm.2022.104564.
[25] Y. Li, H. Jahr, P. Pavanram, F.S.L. Bobbert, U. Puggi, X.Y. Zhang, B. Pouran, M. A. Leeflang, H. Weinans, J. Zhou, A.A. Zadpoor, Additively manufactured functionally graded biodegradable porous iron, Acta Biomater. 96 (2019) 646–661, https://doi.org/10.1016/j.actbio.2019.07.013.
[26] C. Shuai, W. Yang, Y. Yang, H. Pan, C. He, F. Qi, D. Xie, H. Liang, Selective laser melted Fe-Mn bone scaffold: microstructure, corrosion behavior and cell response, Mater. Res. Express. 7 (2019) 015404, https://doi.org/10.1088/2053-1591/ab62f5.
[27] C. Xu, H. Zhang, S. Yu, W. Wu, L. Zhang, Q. Liu, L. Ren, Direct ink writing of porous Fe scaffolds for bone implants: pore size evolution and effect on degradation and mechanical properties, J. Mater. Res. Technol. 25 (2023) 4901–4912, https://doi.org/10.1016/j.jmrt.2023.06.258.
[28] N.E. Putra, M.A. Leeflang, P. Taheri, L.E. Fratila-Apachitei, J.M.C. Mol, J. Zhou, A.A. Zadpoor, Extrusion-based 3D printing of ex situ-alloyed highly biodegradable MRI-friendly porous iron-manganese scaffolds, Acta Biomater. 134 (2021) 774–790, https://doi.org/10.1016/j.actbio.2021.07.042.
[29] C. Shuai, Y. Li, Y. Yang, S. Peng, W. Yang, F. Qi, S. Xiong, H. Liang, L. Shen, Bioceramic enhances the degradation and bioactivity of iron bone implant, Mater. Res. Express. 6 (2019) 115401, https://doi.org/10.1088/2053-1591/ab45b9.
[30] C. Gao, M. Yao, S. Li, P. Feng, S. Peng, C. Shuai, Highly biodegradable and bioactive Fe-Pd-bredigite biocomposites prepared by selective laser melting, J. Adv. Res. 20 (2019) 91–104, https://doi.org/10.1016/j.jare.2019.06.001.
[31] C. Xu, M. Ban, H. Zhang, Q. Liu, L. Ren, Direct ink writing of porous Fe-HA metal-matrix composites (MMCs) with independently adjustable porosity and degradation rate for bone implant applications, Mater. Des. 224 (2022) 111319, https://doi.org/10.1016/j.matdes.2022.111319.
[32] N.E. Putra, K.G.N. Borg, P.J. Diaz-Payno, M.A. Leeflang, M. Klimopoulou, P. Taheri, J.M.C. Mol, L.E. Fratila-Apachitei, Z. Huan, J. Chang, J. Zhou, A. A. Zadpoor, Additive manufacturing of bioactive and biodegradable porous iron-akermanite composites for bone regeneration, Acta Biomater. 148 (2022) 355–373, https://doi.org/10.1016/j.actbio.2022.06.009.
[33] R.J. Morrison, K.N. Kashlan, C.L. Flanangan, J.K. Wright, G.E. Green, S. J. Hollister, K.J. Weatherwax, Regulatory considerations in the design and manufacturing of implantable 3D-printed medical devices, Clin. Transl. Sci. 8 (2015) 594–600, https://doi.org/10.1111/cts.12315.
[34] M. Cheng, W. Liu, J. Zhang, S. Zhang, Z. Guo, L. Liu, J. Tian, X. Zhang, J. Cheng, Y. Liu, G. Deng, G. Gao, L. Sun, Regulatory considerations for animal studies of biomaterial products, Bioact. Mater. 11 (2022) 52–56, https://doi.org/10.1016/j.bioactmat.2021.09.031.
[35] S. Kooner, C. Hewison, S. Sridharan, J. Lui, G. Matthewson, H. Johal, M. Clark, Waste and recycling among orthopedic subspecialties, Can. J. Surg. 63 (2020) E278–E283, https://doi.org/10.1503/CJS.018018.
[36] K.M. Phoon, I. Afzal, D.H. Sochart, V. Asopa, P. Gikas, D. Kader, Environmental sustainability in orthopaedic surgery: a scoping review, Bone Jt. Open. 3 (2022) 628–640, https://doi.org/10.1302/2633-1462.38.BJO-2022-0067.R1.
[37] A. Peys, V. Isteri, J. Yliniemi, A.S. Yorkshire, P.N. Lemougna, C. Utton, J.L. Provis, R. Snellings, T. Hanein, Sustainable iron-rich cements: raw material sources and binder types, Cem. Concr. Res. 157 (2022) 106834, https://doi.org/10.1016/j.cemconres.2022.106834.
[38] L.S. Teseletso, T. Adachi, Long-term sustainability of copper and iron based on a system dynamics model, Resources 11 (2022) 37, https://doi.org/10.3390/resources11040037.
[39] D. Raabe, C.C. Tasan, E.A. Olivetti, Strategies for improving the sustainability of structural metals, Nature 575 (2019) 64–74, https://doi.org/10.1038/s41586-019-1702-5.
[40] A. Laca, A. Laca, M. Díaz, Eggshell waste as catalyst: a review, J. Environ. Manag. 197 (2017) 351–359, https://doi.org/10.1016/j.jenvman.2017.03.088.
[41] M. Waheed, M. Yousaf, A. Shehzad, M. Inam-Ur-Raheem, M.K.I. Khan, M.R. Khan, N. Ahmad, R.M.A. Abdullah, Channelling eggshell waste to valuable and utilizable products: a comprehensive review, Trends Food Sci. Technol. 106 (2020) 78–90, https://doi.org/10.1016/j.tifs.2020.10.009.

[42] T.S.S. Kumar, K. Madhumathi, R. Jayasree, Eggshell waste: a gold mine for sustainable bioceramics, J. Indian Inst. Sci. 102 (2022) 599–620, https://doi.org/10.1007/s41745-022-00291-3.

[43] X. Wu, S.I. Stroll, D. Lantigua, S. Suvarnapathaki, G. Camci-Unal, Eggshell particle-reinforced hydrogels for bone tissue engineering: an orthogonal approach, Biomater. Sci. 7 (2019) 2675–2685, https://doi.org/10.1039/c9bm00230h.

[44] X. Wu, O. Gauntlett, T. Zhang, S. Suvarnapathaki, C. Mccarthy, B. Wu, G. Camci-Unal, Eggshell microparticle reinforced scaffolds for regeneration of critical sized cranial defects, ACS Appl. Mater. Interfaces. 13 (2021) 60921–60932, https://doi.org/10.1021/acsami.1c19884.

[45] S. Shafiei, M. Omidi, F. Nasehi, H. Golzar, D. Mohammadrezaei, M. Rezai Rad, A. Khojasteh, Egg shell-derived calcium phosphate/carbon dot nanofibrous scaffolds for bone tissue engineering: fabrication and characterization, Mater. Sci. Eng. C. 100 (2019) 564–575, https://doi.org/10.1016/j.msec.2019.03.003.

[46] R. Jayasree, T.S.S. Kumar, R. Venkateswari, R.P. Nankar, M. Doble, Eggshell derived brushite bone cement with minimal inflammatory response and higher osteoconductive potential, J. Mater. Sci. Mater. Med. 30 (2019) 1–4, https://doi.org/10.1007/s10856-019-6315-x.

[47] R. Domander, A.A. Felder, M. Doube, D. Schmidt, BoneJ2 - refactoring established research software, Wellcome Open Res. (2021) 1–21.

[48] ASTM B963-17, Standard test methods for oil content, oil-impregnation efficiency, and surface-connected porosity of sintered powder metallurgy (PM) products using Archimedes' principle, ASTM International, 2017, https://doi.org/10.1520/B0963-14.

[49] A. Oyane, H.M. Kim, T. Furuya, T. Kokubo, T. Miyazaki, T. Nakamura, Preparation and assessment of revised simulated body fluids, J. Biomed. Mater. Res. - Part A. 65 (2003) 188–195, https://doi.org/10.1002/jbm.a.10482.

[50] L. Yang, E. Zhang, Biocorrosion behavior of magnesium alloy in different simulated fluids for biomedical application, Mater. Sci. Eng. C. 29 (2009) 1691–1696, https://doi.org/10.1016/j.msec.2009.01.014.

[51] ASTM G1-03, Standard practice for preparing, cleaning, and evaluating corrosion test specimens, ASTM Int, 2017, https://doi.org/10.1520/G0001-03R17E01.2.

[52] N.E. Putra, A. Tigrine, S. Aksakal, V.R. de la Rosa, P. Taheri, L.E. Fratila-Apachitei, J.M.C. Mol, J. Zhou, A.A. Zadpoor, Poly(2-ethyl-2-oxazoline) coating of additively manufactured biodegradable porous iron, Biomater. Adv. 133 (2022) 112617, https://doi.org/10.1016/j.msec.2021.112617.

[53] ASTM G31-72, Standard practice for laboratory immersion corrosion testing of metals, ASTM Int, 2004, https://doi.org/10.1520/G0031-72R04.2.

[54] ISO 13314, Mechanical testing of metals - Ductility testing - Compression test for porous and cellular metals, Int. Organ. Stand., 2011. www.iso.org.

[55] T.F. Moriarty, D. Campoccia, S.K. Nees, L.P. Boure, R.G. Richards, In vivo evaluation of the effect of intramedullary nail microtopography on the development of local infection in rabbits, Int. J. Artif. Organs. 33 (2010) 667–675, https://doi.org/10.1177/039139881003300913.

[56] D. Campoccia, L. Montanaro, T.F. Moriarty, R.G. Richards, S. Ravaioli, C. R. Arciola, The selection of appropriate bacterial strains in preclinical evaluation of infection-resistant biomaterials, Int. J. Artif. Organs. 31 (2008) 841–847, https://doi.org/10.1177/039139880803100913.

[57] E.M. Haisma, A. De Breij, H. Chan, J.T. Van Dissel, J.W. Drijfhout, P.S. Hiemstra, A. El Ghalbzouri, P.H. Nibbering, LL-37-derived peptides eradicate multidrug-resistant Staphylococcus aureus from thermally wounded human skin equivalents, Antimicrob. Agents Chemother. 58 (2014) 4411–4419, https://doi.org/10.1128/AAC.02554-14.

[58] JIS Z 2801, Antimicrobial products - Test for antimicrobial activity and efficacy, Japanese Ind. Stand, 2000.

[59] E.F. Morgan, G.U. Unnikrisnan, A.I. Hussein, Bone mechanical properties in healthy and diseased states, Annu. Rev. Biomed. Eng. 20 (2018) 119–143, https://doi.org/10.1146/annurev-bioeng-062117-121139.

[60] C. Xu, Y. Xu, H. Chen, Q. Han, W. Wu, L. Zhang, Q. Liu, J. Wang, L. Ren, Novel-ink-based direct ink writing of Ti6Al4V scaffolds with sub-300 μm structural pores for superior cell proliferation and differentiation, Adv. Healthc. Mater. 2302396 (2024) 1–14, https://doi.org/10.1002/adhm.202302396.

[61] V.G. Rocha, E. Saiz, I.S. Tirichenko, E. García-Tuñón, Direct ink writing advances in multi-material structures for a sustainable future, J. Mater. Chem. A. 8 (2020) 15646–15657, https://doi.org/10.1039/d0ta04181e.

[62] M.A.S.R. Saadi, A. Maguire, N.T. Pottackal, M.S.H. Thakur, M.M. Ikram, A. J. Hart, P.M. Ajayan, M.M. Rahman, Direct ink writing: a 3D printing technology for diverse materials, Adv. Mater. 34 (2022) 2108855, https://doi.org/10.1002/adma.202108855.

[63] E.B. Montufar, M. Casas-Luna, M. Horynová, S. Tkachenko, Z. Fohlerová, S. Diaz-de-la-Torre, K. Dvořák, L. Čelko, J. Kaiser, High strength, biodegradable and cytocompatible alpha tricalcium phosphate-iron composites for temporal reduction of bone fractures, Acta Biomater. 70 (2018) 293–303, https://doi.org/10.1016/j.actbio.2018.02.002.

[64] M. Heiden, E. Nauman, L. Stanciu, Bioresorbable Fe–Mn and Fe–Mn–HA materials for orthopedic implantation: enhancing degradation through porosity control, Adv. Healthc. Mater. 6 (2017) 1–12, https://doi.org/10.1002/adhm.201700120.

[65] A. Reindl, R. Borowsky, S.B. Hein, J. Geis-Gerstorfer, P. Imgrund, F. Petzoldt, Degradation behavior of novel Fe/ß-TCP composites produced by powder injection molding for cortical bone replacement, J. Mater. Sci. 49 (2014) 8234–8243, https://doi.org/10.1007/s10853-014-8532-5.

[66] M.F. Ulum, A. Arafat, D. Noviana, A.H. Yusop, A.K. Nasution, M.R. Abdul Kadir, H. Hermawan, In vitro and in vivo degradation evaluation of novel iron-bioceramic composites for bone implant applications, Mater. Sci. Eng. C. 36 (2014) 336–344, https://doi.org/10.1016/j.msec.2013.12.022.

[67] S. Wang, Y. Xu, J. Zhou, H. Li, J. Chang, Z. Huan, In vitro degradation and surface bioactivity of iron-matrix composites containing silicate-based bioceramic, Bioact. Mater. 2 (2017) 10–18, https://doi.org/10.1016/j.bioactmat.2016.12.001.

[68] N. Jmal, J. Bouaziz, Synthesis, characterization and bioactivity of a calcium-phosphate glass-ceramics obtained by the sol-gel processing method, Mater. Sci. Eng. C. 71 (2017) 279–288, https://doi.org/10.1016/j.msec.2016.09.058.

[69] S. Sakthi Muthulakshmi, S. Shailajha, B. Shanmugapriya, Bio-physical investigation of calcium silicate biomaterials by green synthesis- osseous tissue regeneration, J. Mater. Res. 38 (2023) 4369–4384, https://doi.org/10.1557/s43578-023-01149-9.

[70] L. Dupoirieux, D. Pourquier, F. Souyris, Powdered eggshell: A pilot study on a new bone substitute for use in maxillofacial surgery, J. Cranio-Maxillofac. Surg. 23 (1995) 187–194, https://doi.org/10.1016/S1010-5182(05)80009-5.

[71] M. Sayed, H.F. El-Maghraby, F. Bondioli, S.M. Naga, 3D carboxymethyl cellulose/hydroxyapatite (CMC/HA) scaffold composites based on recycled eggshell, J. Appl. Pharm. Sci. 8 (2018) 23–30, https://doi.org/10.7324/JAPS.2018.8304.

[72] U.K. Roopavath, M.K. Sah, B.B. Panigrahi, S.N. Rath, Mechanochemically synthesized phase stable and biocompatible β-tricalcium phosphate from avian eggshell for the development of tissue ingrowth system, Ceram. Int. 45 (2019) 12910–12919, https://doi.org/10.1016/j.ceramint.2019.03.217.

[73] P. Dadhich, B. Das, P. Pal, P.K. Srivas, J. Dutta, S. Ray, S. Dhara, A simple approach for an eggshell-based 3D-printed osteoinductive multiphasic calcium phosphate scaffold, ACS Appl. Mater. Interfaces. 8 (2016) 11910–11924, https://doi.org/10.1021/acsami.5b11981.

[74] N. Raja, A. Sung, H. Park, H.S. Yun, Low-temperature fabrication of calcium deficient hydroxyapatite bone scaffold by optimization of 3D printing conditions, Ceram. Int. 47 (2021) 7005–7016, https://doi.org/10.1016/j.ceramint.2020.11.051.

[75] C.F. Marques, F.H. Perera, A. Marote, S. Ferreira, S.I. Vieira, S. Olhero, P. Miranda, J.M.F. Ferreira, Biphasic calcium phosphate scaffolds fabricated by direct write assembly: mechanical, anti-microbial and osteoblastic properties, J. Eur. Ceram. Soc. 37 (2017) 359–368, https://doi.org/10.1016/j.jeurceramsoc.2016.08.018.

[76] L. del-Mazo-Barbara, M.P. Ginebra, Rheological characterisation of ceramic inks for 3D direct ink writing: a review, J. Eur. Ceram. Soc. 41 (2021) 18–33, https://doi.org/10.1016/j.jeurceramsoc.2021.08.031.

[77] C. Torres-Sanchez, M. Norrito, F.R. Almushref, P.P. Conway, The impact of multimodal pore size considered independently from porosity on mechanical performance and osteogenic behaviour of titanium scaffolds, Mater. Sci. Eng. C. 124 (2021) 112026, https://doi.org/10.1016/j.msec.2021.112026.

[78] M. Paris, A. Götz, I. Hettrich, C.M. Bidan, J.W.C. Dunlop, H. Razi, I. Zizak, D. W. Hutmacher, P. Fratzl, G.N. Duda, W. Wagermaier, A. Cipitria, Scaffold curvature-mediated novel biomineralization process originates a continuous soft tissue-to-bone interface, Acta Biomater. 60 (2017) 64–80, https://doi.org/10.1016/j.actbio.2017.07.029.

[79] T. Hidayat, D. Shishin, S.A. Decterov, E. Jak, Thermodynamic optimization of the Ca-Fe-O system, Metall. Mater. Trans. B Process Metall. Mater. Process. Sci. 47 (2016) 256–281, https://doi.org/10.1007/s11663-015-0501-0.

[80] A. Mostafaei, P. Rodriguez De Vecchis, I. Nettleship, M. Chmielus, Effect of powder size distribution on densification and microstructural evolution of binder-jet 3D-printed alloy 625, Mater. Des. 162 (2019) 375–383, https://doi.org/10.1016/j.matdes.2018.11.051.

[81] W. Du, J. Roa, J. Hong, Y. Liu, Z. Pei, C. Ma, Binder jetting additive manufacturing: effect of particle size distribution on density, J. Manuf. Sci. Eng. Trans. ASME. 143 (2021) 1–9, https://doi.org/10.1115/1.4050306.

[82] R.A. Gittens, T. McLachlan, R. Olivares-Navarrete, Y. Cai, S. Berner, R. Tannenbaum, Z. Schwartz, K.H. Sandhage, B.D. Boyan, The effects of combined micron-/submicron-scale surface roughness and nanoscale features on cell proliferation and differentiation, Biomaterials 32 (2011) 3395–3403, https://doi.org/10.1016/j.biomaterials.2011.01.029.

[83] C. Shuai, S. Li, S. Peng, P. Feng, Y. Lai, C. Gao, Biodegradable metallic bone implants, Mater. Chem. Front. 3 (2019) 544–562, https://doi.org/10.1039/c8qm00507a.

[84] H. Ma, T. Li, Z. Huan, M. Zhang, Z. Yang, J. Wang, J. Chang, C. Wu, 3D printing of high-strength bioscaffolds for the synergistic treatment of bone cancer, NPG Asia Mater. 10 (2018) 31–44, https://doi.org/10.1038/s41427-018-0015-8.

[85] D.R. Lide, Solubility Product Constants in CRC Handbook of Chemistry and Physics, 87th ed., CRC Press, Boca Raton, Florida, 2006. http://www2.chm.ulaval.ca/gecha/chm1903/6_solubilite_solides/solubility_products.pdf.

[86] A. Xu, F. Zhang, F. Jin, R. Zhang, B. Luo, T. Zhang, The evaluation of coating performance by analyzing the intersection of Bode plots, Int. J. Electrochem. Sci. 9 (2014) 5125.

[87] D. You, N. Pebere, F. Dabosi, An investigation of the corrosion of pure iron by electrochemical techniques and in situ observations, Corros. Sci. 34 (1993) 5–15, https://doi.org/10.1016/0010-938X(93)90254-E.

[88] P. Sharma, P.M. Pandey, Corrosion behaviour of the porous iron scaffold in simulated body fluid for biodegradable implant application, Mater. Sci. Eng. C. 99 (2019) 838–852, https://doi.org/10.1016/j.msec.2019.01.114.

[89] J. Zhou, Y. Yang, M.A. Frank, R. Detsch, A.R. Boccaccini, S. Virtanen, Accelerated degradation behavior and cytocompatibility of pure iron treated with sandblasting, ACS Appl. Mater. Interfaces. 8 (2016) 26482–26492, https://doi.org/10.1021/acsami.6b07068.

[90] M. Mozafari, S. Banijamali, F. Baino, S. Kargozar, R.G. Hill, Calcium carbonate: adored and ignored in bioactivity assessment, Acta Biomater. 91 (2019) 35–47, https://doi.org/10.1016/j.actbio.2019.04.039.

[91] L. Müller, F.A. Müller, Preparation of SBF with different HCO3- content and its influence on the composition of biomimetic apatites, Acta Biomater. 2 (2006) 181–189, https://doi.org/10.1016/j.actbio.2005.11.001.
[92] X.B. Chen, Y.C. Li, J. Du Plessis, P.D. Hodgson, C. Wen, Influence of calcium ion deposition on apatite-inducing ability of porous titanium for biomedical applications, Acta Biomater. 5 (2009) 1808–1820, https://doi.org/10.1016/j.actbio.2009.01.015.
[93] S.Y. Yang, H.H. Chang, C.J. Lin, S.J. Huang, J.C.C. Chan, Is Mg-stabilized amorphous calcium carbonate a homogeneous mixture of amorphous magnesium carbonate and amorphous calcium carbonate? Chem. Commun. 52 (2016) 11527–11530, https://doi.org/10.1039/c6cc04522g.
[94] J. Zhang, C. Dong, Y. Sun, J. Yu, Mechanism of magnesium's influence on calcium carbonate crystallization: kinetically controlled multistep crystallization, Cryst. Res. Technol. 53 (2018) 1–8, https://doi.org/10.1002/crat.201800075.
[95] M. Kellermeier, E. Melero-García, F. Glaab, R. Klein, M. Drechsler, R. Rachel, J. M. García-Ruiz, W. Kunz, Stabilization of amorphous calcium carbonate in inorganic silica-rich environments, J. Am. Chem. Soc. 132 (2010) 17859–17866, https://doi.org/10.1021/ja106959p.
[96] W.E.G. Müller, M. Neufurth, J. Huang, K. Wang, Q. Feng, H.C. Schröder, B. Diehl-Seifert, R. Muñoz-Espí, X. Wang, Nonenzymatic transformation of amorphous CaCO3 into calcium phosphate mineral after exposure to sodium phosphate in vitro: implications for in vivo hydroxyapatite bone formation, ChemBioChem 16 (2015) 1323–1332, https://doi.org/10.1002/cbic.201500057.
[97] Y. Li, K. Lietaert, W. Li, X.Y. Zhang, M.A. Leeflang, J. Zhou, A.A. Zadpoor, Corrosion fatigue behavior of additively manufactured biodegradable porous iron, Corros. Sci. 156 (2019) 106–116, https://doi.org/10.1016/j.corsci.2019.05.003.
[98] N.E. Putra, V. Moosabeiki, M.A. Leeflang, J. Zhou, A.A. Zadpoor, Biodegradation-affected fatigue behavior of extrusion-based additively manufactured porous iron–manganese scaffolds, Acta Biomater. 178 (2024) 340–351, https://doi.org/10.1016/j.actbio.2024.02.024.
[99] Y. Li, H. Jahr, X.Y. Zhang, M.A. Leeflang, W. Li, B. Pouran, F.D. Tichelaar, H. Weinans, J. Zhou, A.A. Zadpoor, Biodegradation-affected fatigue behavior of additively manufactured porous magnesium, Addit. Manuf. 28 (2019) 299–311, https://doi.org/10.1016/j.addma.2019.05.013.
[100] K. Slámečka, A. Kashimbetova, J. Pokluda, T. Zikmund, J. Kaiser, E.B. Montufar, L. Čelko, Fatigue behaviour of titanium scaffolds with hierarchical porosity produced by material extrusion additive manufacturing, Mater. Des. 225 (2023) 111453, https://doi.org/10.1016/j.matdes.2022.111453.
[101] B.R. Merk, S.H. Stern, S. Cordes, E.P. Lautenschlager, A fatigue life analysis of small fragment screws, J. Orthop. Trauma. 15 (2001) 494–499, https://doi.org/10.1097/00005131-200109000-00006.
[102] S.M. Hou, J.L. Wang, J. Lin, Mechanical strength, fatigue life, and failure analysis of two prototypes and five conventional tibial locking screws, J. Orthop. Trauma. 16 (2002) 701–708, https://doi.org/10.1097/00005131-200211000-00004.
[103] Y. Li, W. Li, F.S.L. Bobbert, K. Lietaert, J.H. Dong, M.A. Leeflang, J. Zhou, A. A. Zadpoor, Corrosion fatigue behavior of additively manufactured biodegradable porous zinc, Acta Biomater. 106 (2020) 439–449, https://doi.org/10.1016/j.actbio.2020.02.001.
[104] I.A.J. van Hengel, N.E. Putra, M.W.A.M. Tierolf, M. Minneboo, A.C. Fluit, L. E. Fratila-Apachitei, I. Apachitei, A.A. Zadpoor, Biofunctionalization of selective laser melted porous titanium using silver and zinc nanoparticles to prevent infections by antibiotic-resistant bacteria, Acta Biomater. 107 (2020) 325–337, https://doi.org/10.1016/j.actbio.2020.02.044.
[105] N.E. Putra, M.A. Leeflang, V. Ducret, V. Patrulea, L.E. Fratila-Apachitei, K. Perron, H. Ye, J. Zhou, I. Apachitei, A.A. Zadpoor, Preventing antibiotic-resistant infections: additively manufactured porous Ti6Al4V biofunctionalized with Ag and Fe nanoparticles, Int. J. Mol. Sci. 23 (2022) 13239, https://doi.org/10.3390/ijms232113239.
[106] Y.L. Li, J. He, H.X. Ye, C.C. Zhao, W.W. Zhu, X. Lu, F.Z. Ren, Atomic layer deposition of zinc oxide onto 3D porous iron scaffolds for bone repair: in vitro degradation, antibacterial activity and cytocompatibility evaluation, Rare Met. (2021) 18–22, https://doi.org/10.1007/s12598-021-01852-8.
[107] P. Sotoudehbagha, S. Sheibani, M. Khakbiz, S. Ebrahimi-Barough, H. Hermawan, Novel antibacterial biodegradable Fe-Mn-Ag alloys produced by mechanical alloying, Mater. Sci. Eng. C. 88 (2018) 88–94, https://doi.org/10.1016/j.msec.2018.03.005.
[108] S. Mandal, V. Kishore, M. Bose, S.K. Nandi, M. Roy, In vitro and in vivo degradability, biocompatibility and antimicrobial characteristics of Cu added iron-manganese alloy, J. Mater. Sci. Technol. 84 (2021) 159–172, https://doi.org/10.1016/j.jmst.2020.12.029.
[109] J. Sawai, Quantitative evaluation of antibacterial activities of metallic oxide powders (ZnO, MgO and CaO) by conductimetric assay, J. Microbiol. Methods. 54 (2003) 177–182, https://doi.org/10.1016/S0167-7012(03)00037-X.
[110] C. Silva, F. Bobillier, D. Canales, F.A. Sepúlveda, A. Cament, N. Amigo, L. M. Rivas, M.T. Ulloa, P. Reyes, J.A. Ortiz, T. Gómez, C. Loyo, P.A. Zapata, Mechanical and antimicrobial polyethylene composites with CaO nanoparticles, Polymers (Basel) 12 (2020) 2132, https://doi.org/10.3390/POLYM12092132.
[111] C. Loyo, V. Moreno-Serna, J. Fuentes, N. Amigo, F.A. Sepúlveda, J.A. Ortiz, L. M. Rivas, M.T. Ulloa, R. Benavente, P.A. Zapata, PLA/CaO nanocomposites with antimicrobial and photodegradation properties, Polym. Degrad. Stab. 197 (2022) 109865, https://doi.org/10.1016/j.polymdegradstab.2022.109865.
[112] M. Croes, S. Bakhshandeh, I.A.J. van Hengel, K. Lietaert, K.P.M. van Kessel, B. Pouran, B.C.H. van der Wal, H.C. Vogely, W. Van Hecke, A.C. Fluit, C.H.E. Boel, J. Alblas, A.A. Zadpoor, H. Weinans, S.A. Yavari, Antibacterial and immunogenic behavior of silver coatings on additively manufactured porous titanium, Acta Biomater. 81 (2018) 315–327, https://doi.org/10.1016/j.actbio.2018.09.051.
[113] B.I.M. Eijkel, I. Apachitei, L.E. Fratila-Apachitei, A.A. Zadpoor, In vitro co-culture models for the assessment of orthopedic antibacterial biomaterials, Front. Bioeng. Biotechnol. 12 (2024) 1–11, https://doi.org/10.3389/fbioe.2024.1332771.
[114] M. Zayzafoon, Calcium/calmodulin signaling controls osteoblast growth and differentiation, J. Cell. Biochem. 97 (2006) 56–70, https://doi.org/10.1002/jcb.20675.
[115] H. Cheng, H. Hu, G. Li, M. Zhang, K. Xiang, Z. Zhu, Y. Wan, Calcium titanate micro-sheets scaffold for improved cell viability and osteogenesis, Chem. Eng. J. 389 (2020) 124400, https://doi.org/10.1016/j.cej.2020.124400.
[116] Z. Li, X. Zhang, J. Ouyang, D. Chu, F. Han, L. Shi, R. Liu, Z. Guo, G.X. Gu, W. Tao, L. Jin, J. Li, Ca2+-supplying black phosphorus-based scaffolds fabricated with microfluidic technology for osteogenesis, Bioact. Mater. 6 (2021) 4053–4064, https://doi.org/10.1016/j.bioactmat.2021.04.014.
[117] J. Zhang, Y. Ji, S. Jiang, M. Shi, W. Cai, R.J. Miron, Y. Zhang, Calcium-collagen coupling is vital for biomineralization schedule, Adv. Sci. 8 (2021) 1–15, https://doi.org/10.1002/advs.202100363.
[118] E. Holm, J.S. Gleberzon, Y. Liao, E.S. Sørensen, F. Beier, G.K. Hunter, H. A. Goldberg, Osteopontin mediates mineralization and not osteogenic cell development in vitro, Biochem. J. 464 (2014) 355–364, https://doi.org/10.1042/BJ20140702.
[119] Y.T. Tsao, Y.J. Huang, H.H. Wu, Y.A. Liu, Y.S. Liu, O.K. Lee, Osteocalcin mediates biomineralization during osteogenic maturation in human mesenchymal stromal cells, Int. J. Mol. Sci. 18 (2017) 159, https://doi.org/10.3390/ijms18010159.